ISSP

Activity Report 2003

Contents

Pages

Preface

The ISSP was established in 1957 based on the recommendation of the National Council of Japan to set up a new institute for condensed matter physics. The idea was to establish a top class research institute for experimental and theoretical studies of condensed matter and to promote cooperative research in the field throughout the country. Soon after the inauguration, the name of ISSP became recognized world-wide in the community of condensed matter physics.

Since then there have been two major changes in the history of the institute. The first was the reorganization of the institute in the mid-eighties. The system of divisions consisting of several groups was introduced and the project of the "Physics in extreme conditions", which includes Ultra-High Magnetic Fields, Laser Physics, Surface Physics, Ultra-Low Temperatures, and Very High Pressures, was started. The second major change was the relocation of the ISSP to the new Kashiwa campus which was completed in 2000.

To make the status of the research activities public, new forms were introduced two years ago: Activity report A for research mostly by the staff of the ISSP and Activity report B for joint research conducted by the ISSP. This is the Activity Report for the fiscal year 2003 in the style of single volume with all the research activities at the ISSP. The system of national universities in Japan has made a profound change from April first this year by the so called "houjinka", which means that national universities, once directly belonged to the ministry of education, have become independent administrative entities. In the new scheme importance of the Activity Report will be enhanced.

We are happy to receive any comments on the Report for the possible improvement of the research activities of the ISSP.

June 18, 2004
Kazuo Ueda
Director
Institute for Solid State Physics
The University of Tokyo

Research Highlights

Pressure Induced Phase Transformation in Hollandite-type $KAlSi_3O_8$

T. Yagi

We have found a pressure induced phase transformation in $KAlSi_3O_8$ at around 20 GPa and room temperature. Hollandite structured $KAlSi_3O_8$ is believed to be one of the important constituent minerals of subducting slab in the Earth. In spite of the close packing of atoms, hollandite-type structure can accommodate large cations such as potassium. Among various silicates, there are not so many structures which can accommodate such large cation under pressure. Therefore its behavior under deep Earth condition has geophysical importance for the discussion of the distribution of potassium and hence the thermal history of the Earth, because the radioactive decay of potassium is the main heat source in the deep Earth. Moreover, its unique structure attracts attention from a view point of materials science as well.

We have carried out high pressure in situ X-ray diffraction study on hollandite structured $KAlSi_3O_8$ up to 28 GPa at room temperature, using helium as a pressure transmitting medium. Helium provides nearly hydrostatic environment and, as a results, high quality X-ray diffraction profiles were obtained under pressure. Starting sample was prepared from a stoichiometric mixture of oxides heated to 1800K at about 20 GPa using multi-anvil apparatus and the X-ray diffraction experiments were carried out at BL13 of the Photon Factory. Fig. 1 shows series of X-ray diffraction profiles obtained with increasing pressure. Contrary to the previous report [1], the existence of a phase transformation was found at around 20 GPa, which occurs reversibly at room temperature. Analysis of the diffraction pattern above 20 GPa indicates the transformation from tetragonal to monoclinic structure. Hollandite-type structure has several modifications. Original hollandite, $BaMn_8O_{16}$, has monoclinic symmetry while hollandite-type $KAlSi_3O_8$ has tetragonal symmetry at low pressure. Above 20 GPa, however, it distorts into monoclinic structure. In Fig. 2, the change of the angle γ of the unit cell is shown as a function of pressure. It is clear from this figure that the tetragonal unit cell starts to distort at about 20 GPa. If we look at the unit cell dimensions, *a*-axis splits into *a*- and *b*-axis at the transition while *c*-axis changes almost continuously across the transition. No meaningful discontinuous change in volume was found at the transition and no hysteresis of the transition pressure was found in increasing and decreasing pressure cycle. All these facts suggest that the nature of this transition is a second order structural transition. Hollandite structure has one dimensional "tunnel" along *c*-axis in which large cation is sitting and this tunnel is deformed at the transition. Therefore, although the density is affected only little by this transition, it is likely that the partitioning of large elements which is contained in this tunnel may be affected considerably below and above the transition. Various physical properties may be affected by this transition as well and further studies are required to clarify these problems.

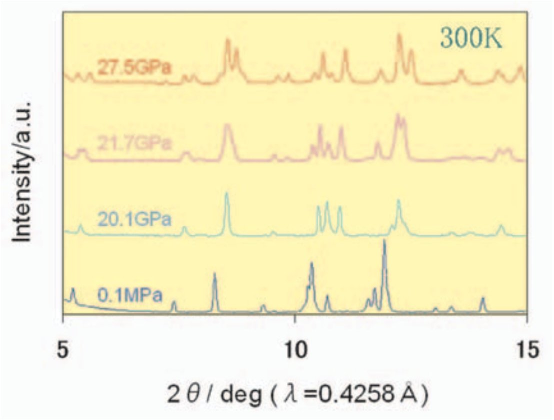

Fig. 1. X-ray diffraction profiles of hollandite-type $KAlSi_3O_8$ under pressure. Many peaks of the original tetragonal structure splits into two ore more peaks above about 20 GPa.

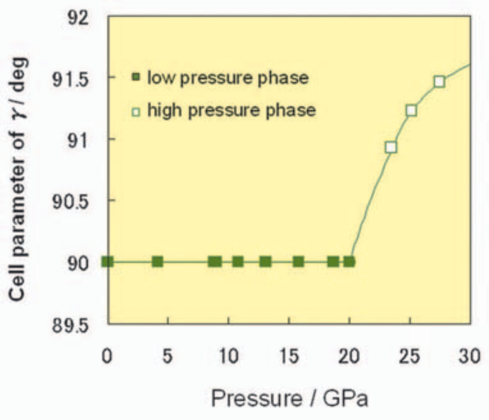

Fig. 2. Change of the unit cell angle γ of hollandite-type $KAlSi_3O_8$ under pressure. At the transition, γ starts to deviate from 90 deg and the distortion increases with increasing pressure .

Reference

[1] F. Tutti, L.S. Dubrovinsky, S.K. Saxena, Geophys. Res. Lett., **28**, 2735 (2001)

Authors
T. Ferroir, T. Onozawa, T. Yagi, S. Merkel, N. Miyajima
M. Nishiyama[a], T. Irifune[a], and T. Kikegawa[b]
[a] Ehime University
[b] Photon Factory, KEK

The Antiferro-Quadrupole Order and the Field-Induced Heavy-Fermion State in the Filled Skutterudite PrFe$_4$P$_{12}$

M. Takigawa

In some rare-earth compounds, high-order multipoles such as electric quadrupoles and magnetic octupoles of the 4*f*-electrons play important roles in determining the electric and magnetic properties. Recently, intermetallic compounds with the filled skutterudite structure, RT_4X_{12} (R = rare earth, T = transition metal, X = pnictogen), have attracted much attention because of a variety of intriguing phenomena in the common lattice structure. Among them, PrFe$_4$P$_{12}$ is unique in that the ground state is nonmagnetic but ordered, with the critical temperature T_A = 6.5 K at zero field. It transforms into a non-ordered heavy-fermion state by applying magnetic field [1]. The low-field phase is suggested to be an antiferro-quadrupole ordered state, however, there is little evidence for the associated change of Pr-4*f* orbitals. Nuclear magnetic resonance (NMR) is a powerful tool to detect such a local change of the electronic state via the hyperfine field at the probed nuclear sites. In order to know more about the ordered phase as well as the heavy-fermion phase at high fields, we carried out NMR measurements at the P site in PrFe$_4$P$_{12}$.

Figure 1(a) shows ^{31}P NMR spectra above and below T_A. The splitting of the NMR lines in the ordered phase indicates existence of two kinds of P sites with different hyperfine fields below T_A. This cannot be due to an ordinary antiferromagnetic (dipole) order because the splitting appears to vanish at zero-field as shown in Fig. 1(b). It should also be noted that the field dependence of the splitting is different for different sites. This suggests that the transition at T_A is not structural but electronic.

These observations are understood in terms of the antiferro-quadrupole (AFQ) order accompanying alternation of the electronic state of Pr atoms on the corner and body-center sites of the *bcc* lattice. Since this leads to a loss of the translational symmetry from the corner to the body center, the presence of two inequivalent P sites is naturally explained. The Pr-4*f* magnetization induced by the field takes different values on different sites in the AFQ state, giving rise to a field-induced staggered magnetization. The hyperfine couplings between P and Pr atoms also alternate because they depend on the symmetry of Pr-4*f* orbitals. This alternation, as well as the staggered magnetization, result in the staggered component of the hyperfine fields in addition to the uniform one, leading to the field-induced line splitting.

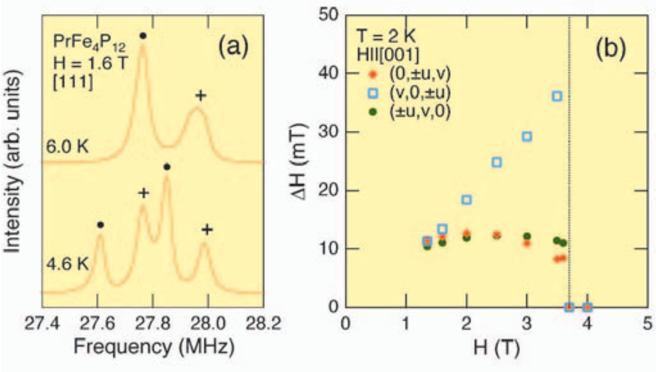

Fig. 1. (a) ^{31}P NMR spectra in PrFe$_4$P$_{12}$ for the field along <111> above and below the transition temperature. Each line splits to a pair of lines (indicated by circles and crosses) in the ordered phase. (b) Field dependence of the line splitting at 2 K for the field along <100>. The dotted line indicates the critical field.

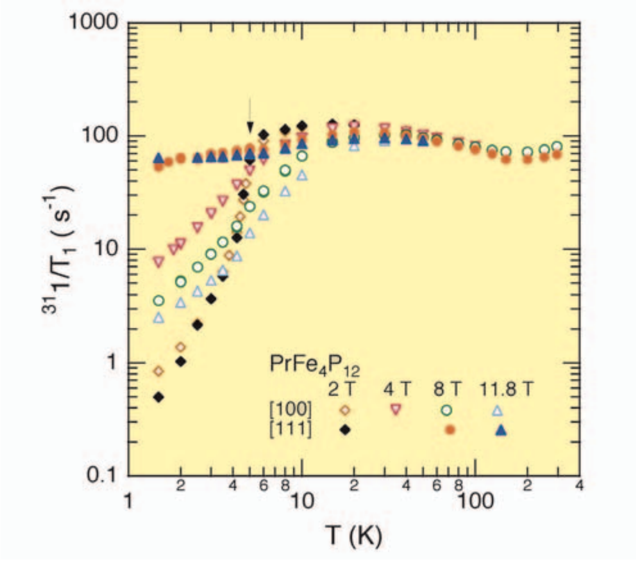

Fig. 2. Temperature and field dependences of the ^{31}P nuclear apin-lattice relaxation rate $1/T_1$ in PrFe$_4$P$_{12}$ for the field ***H*** parallel to <100> and <111>. Open and solid symbols represent $1/T_1$ for ***H***//<100> and <111>, respectively. The arrow indicates the critical temperature of the antiferro-quadrupole order at 2 T.

We found that the main contribution to the line splitting comes from magnetization parallel to the external field ***H***. This allows us to deduce the AFQ order parameter to be dominantly $O_2{}^0$ of the Γ_3 quadrupoles. Further quantitative analyses revealed that the line splitting is determined predominantly by the field-induced staggered octupoles rather than dipoles, which again confirms the AFQ order in the ground state.

On the dynamical side, the ^{31}P nuclear spin-lattice relaxation rate $1/T_1$ decreases rapidly below T_A as shown in Fig. 2 consistent with the nonmagnetic ground state. Anisotropy of $1/T_1$ is relatively small in the AFQ phase. On the other hand, remarkable anisotropy of $1/T_1$ was observed in the high-field heavy-fermion phase. For ***H***//<100>, $1/T_1$ exhibits power-law behavior $1/T_1 \propto T^p$ at low temperatures. The exponent p is field-dependent and approaches one at high fields, suggesting that the Fermi-liquid state is recovered in the high-field limit. In contrast, $1/T_1$ for ***H***//<111> remains enhanced and is almost temperature-independent down to 1.5 K. The enhancement of $1/T_1$ may be related to near degeneracy of the crystal-field levels for ***H***//<111>. This implies a non-Fermi-liquid state due to the quadrupolar Kondo effect, the overscreening process of 4*f*-electron quadrupoles by the conduction electrons [2].

References

[1] H. Sato et al., Physica B **328**, 34 (2003).
[2] D. L. Cox, Phys. Rev. Lett. **59**, 1240 (1987).

Authors
J. Kikuchi, M. Takigawa, H. Sugawara[a], and H. Sato[a]
[a] Tokyo Metropolitan University

Field-angular Oscillation of the Zero-Energy Density of States in the Anisotropic Heavy-Fermion Superconductor CeCoIn$_5$

T. Sakakibara

While the conventional BCS-type superconductors show the superconducting gap opened over the whole Fermi surfaces, anisotropic superconductors are generally characterized by zeros in the gap (either point or line nodes) which break the symmetry of the crystal lattice. Identification of the gap-node structure is therefore of fundamental importance in understanding anisotropic superconductivity and its pairing mechanism. Regarding this issue, it has recently been pointed out that the zero-energy density of states (ZEDOS) in the superconducting mixed state exhibits a characteristic oscillation with respect to the angle between the magnetic field and the nodal directions [1,2]. Experimentally, the angular dependent ZEDOS can be probed by the thermal conductivity or the specific heat measurements in rotating magnetic field at low temperatures. While the former measurement has high sensitivity to the nodal quasiparticles relevant to the phenomenon [3], the latter experiment has an advantage over the former in the point that the interpretation of the result is more straightforward. We have performed the angle-resolved specific heat measurements in the superconducting mixed state of the anisotropic superconductor CeCoIn$_5$ (T_c=2.3 K), and observed a characteristic fourfold angular oscillation in the basal plane.

Figure 1 shows an example of the specific heat data for a single crystal of CeCoIn$_5$, obtained at 0.38 K. The magnetic field of 3 T is rotated in the (001) plane of the tetragonal crystal. As can be seen from the figure, the specific heat shows a characteristic fourfold angular oscillation in the *c*-plane, with the minima (maxima) appearing along the [100] ([110]) directions. The solid line is a fit to a sinusoidal function $\Delta C_H/C_H=A_4\cos(4\theta)$, where C_H denotes the field dependent part of the specific heat. We have done the similar measurements at various temperatures and fields, and found that the relative amplitude A_4 of the angular oscillation persists to low field region H/H_{c2}~0.18, where H_{c2} denotes the upper critical field. We confirmed that A_4 is a decreasing function of magnetic field, and rapidly decreases by raising temperatures up to ~0.5 T_c. These results strongly suggest that the observed angular oscillation comes from the ZEDOS of nodal quasiparticles of *d*-wave superconductivity. From the angular position of the specific-heat minima ([100] directions), we may conclude that the gap symmetry of CeCoIn$_5$ is most likely to be of d_{xy} type.

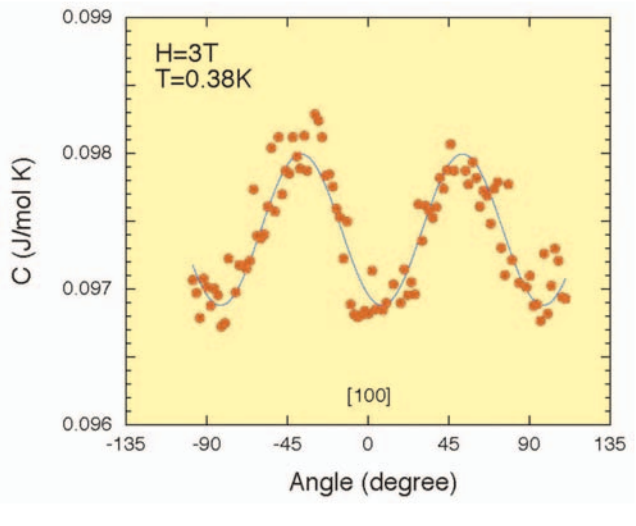

Fig. 1. Specific heat of CeCoIn$_5$ measured at 0.38 K in a magnetic field of 3 T rotated within the (001) plane. The fourfold angular oscillation comes from the gap-node structure of d-wave superconductivity. The field angle is measured with respect to the [100] direction.

References

[1] I. Vekhter et al.: Phys. Rev. B **59** (1999) R9023.
[2] P. Miranovic et al.: Phys. Rev. B **68** (2003) 052501.
[3] K. Izawa et al.: Phys. Rev. Lett. **87** (2001) 057002.

Principal Publication and Authors

J. Phys. Condens. Matter **16** (2004) L13.
H. Aoki, T. Sakakibara, H. Shishido, R. Settai[a], Y. Onuki[a], P. Miranovic[a], and K. Machida[b].
[a] Osaka Univ.
[b] Okayama Univ.

Origin of the Mid-infrared Band in Molecular Conductors

H. Tajima

Optical conductivity spectra of molecular conductors exhibit an intense absorption band in the mid-infrared region (*mid-infrared band*) around room temperature, where their electrical behavior is that of metals or semiconductors with a narrow band gap. This phenomenon has aroused interest of many researchers [1]. In order to understand the mechanism of this phenomenon, we have proposed the following hypothesis [2]:

(i) In some molecular conductors, the original crystal symmetry is broken even at room temperature due to charge ordering (or spin polarization) resulting from the Coulomb repulsion.

(ii) The symmetry breaking due to the Coulomb repulsion is followed by domain formation. Electric current is carried by charged domain walls rather than by single particles.

(iii) The fast time scale of the optical measurement enables one to detect fluctuating order parameters of charge separation or spin polarization. Such parameters are hardly detected by other methods.

This hypothesis relates the mid-infrared band in the conductivity spectra to the charge-ordering phenomena (and to the associated metal-insulator transition) observed in various molecular conductors [3].

Figure 1 shows the optical conductivity spectra of β-(ET)$_2$PF$_6$ above and below the metal-insulator transition temperature ($T_{\text{M-I}}$ =297 K) [4]. The decrease in the conductivity below 1500 cm^{-1} associated with the M-I transition is larger for the polarization parallel to the *a*-axis than for the other polarization. In the insulating phase, the conductivity spectra show a gap feature for the *E*//*a* polarization below 1000 cm^{-1} and a hump appears around 2000~3000 cm^{-1} in the *E*//*c* spectra.

In order to explain the spectral features shown in Fig. 1, we have calculated the optical conductivity spectra by applying the mean-field approximation to the extended Hubbard model. We assumed charge-ordering pattern (shown in Fig. 2a) proposed by Y. Nogami & T. Mori [5].

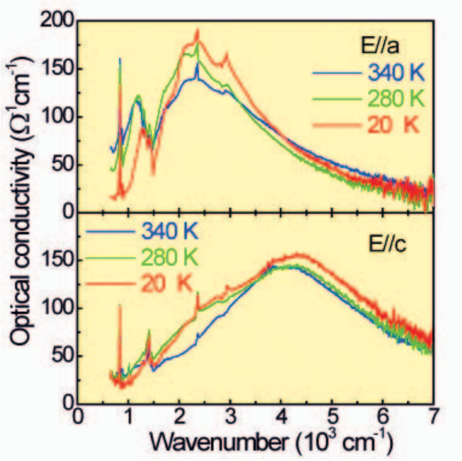

Fig. 1. Infrared conductivity spectra of β-(ET)$_2$PF$_6$ for the polarization parallel to the *a*-axis (top panel) and to the *c*-axis (bottom panel). Note that the spectra exhibit drastic changes associated with the metal-insulator transition at 297 K (=$T_{M\text{-}I}$).

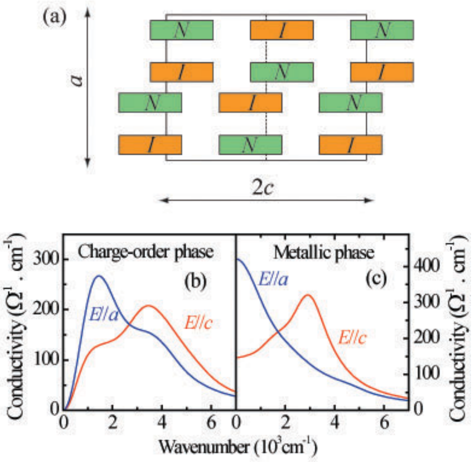

Fig. 2. (a) A schematic pattern of the charge-ordering assumed in the calculation for the insulating phase. The characters *N* and *I* denote neutral and ionic molecules, respectively. (b, c) Conductivity spectra calculated for the charge-order (insulating) and metallic phases.

The spectral features below $T_{\text{M-I}}$ are well explained by this calculation (Fig. 2b). Interestingly, the peak in the *E*//*c* polarization appears even though charge-ordering does not exist (Fig. 2c). *These calculations show that the midinfrared band in the E//a polarization reflects charge-ordering, while the peak in the E//c spectra does not.* This conclusion is consistent with the observed spectra shown in Fig. 1.

References
[1]. For example, see C. S. Jacobsen, in *Semiconductors and Semimetals*, edited by E: Conwell (Academic, London, 1988), Vol. 27, Chap. 5.
[2]. T. Yamamoto, H. Tajima, J. Yamaura, S. Aonuma, and R. Kato, J. Phys. Soc. Jpn., **68**, 1384 (1999); H. Tajima, S. Kyoden, H. Mori, and S. Tanaka, Phys. Rev. B **62**, 9378 (2000).
[3]. For example, see Seo and H. Fukuyama, J. Phys. Soc. Jpn., **66**, 1249 (1997).
[4] Y. Ding and H. Tajima, Phys. Rev. B **69**, 115121 (2004).
[5] Y. Nogami and T. Mori, J. Phys. IV **12**, Pr9-233 (2002).

Authors
H. Tajima and Y. Ding

Construction of Highly Correlated System by the Supramolecular Interaction: κ-type C5DTP-TTF Salts

H. Mori

Generally the electronic states of organic conductors strongly depend upon the molecular arrangements. In the case of ET (bis(ethylenedithio)tetrathiafulvalene) salts, the κ-type structure is very important due to the high superconducting transition temperatures (*Tc*). [1] According to the physical insight, the half-filled band structure, a dimeric structure of 2:1 composition, with the two-dimensional Fermi surface is important to afford the high *Tc*. Then, the donor molecules (CnDTP-TTF in Fig. 1) have been designed for the dimeric structures, so that κ-type and β"-type donor arrangements have been obtained by means of the steric hindrance of the cycloalkylenene group [2] and the intermolecular CH…N interactions of the pyrazino group.

Figure 2 shows the donor arrangement of the κ-(C5DTP-TTF)$_4$GaCl$_4$. The short CH…N contacts of a hydrogen bond (< 2.75 Å) and the steric hindrance of the cyclopentylene group construct the κ-type donor arrangement. The similar behavior was observed for κ-(C5DTP-TTF)$_2$X [X = PF$_6$, AsF$_6$, SbF$_6$].

In order to elucidate the electronic states of the dimeric κ-type and β"-type salts, the electrical resistivities were measured as shown in Fig. 3. A series of the κ-type salts [X = PF$_6$, AsF$_6$, SbF$_6$] show the behavior of Mott insulators with an effective half-filled band. Their spin susceptibilities were also remained even in the insulating state. The metallic regions above 150 K for the PF$_6$ salt and 250 K for the

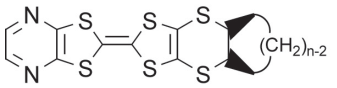

1: C5DTP-TTF (n=5)
2: C6DTP-TTF (n=6)

Fig. 1. Molecular structures of CnDTP-TTF.

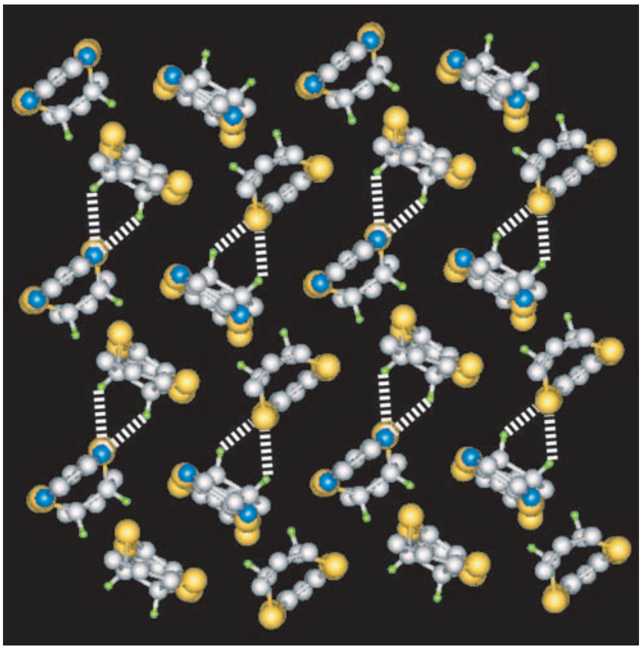

Fig. 2. Crystal structure of κ-(C5DTP-TTF)$_4$GaCl$_4$. The intermolecular CH…N contacts (< 2.75 Å) indicated by the dotted lines and the steric hindrance of the cyclopentylene group construct the κ-type donor arrangement.

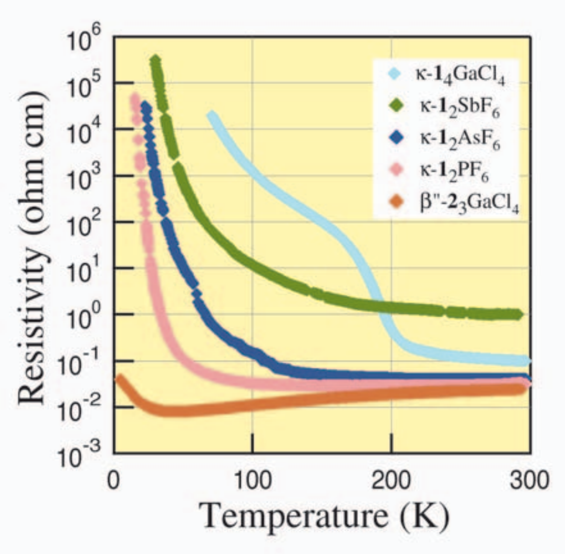

Fig. 3. Temperature dependences of electrical resistivities κ-(C5DTP-TTF)$_2$X [X = PF$_6$, AsF$_6$, SbF$_6$], κ-(C5DTP-TTF)$_4$GaCl$_4$, and β"-(C6DTP-TTF)$_3$GaCl$_4$. A series of the κ-type salts [X = PF$_6$, AsF$_6$, SbF$_6$] are Mott insulators with an effective half-filled band. These resistivity behaviors indicate the chemical pressure effect from the X = SbF$_6$, AsF$_6$, to PF$_6$ salt. In contrast, β"-(C6DTP-TTF)$_3$GaCl$_4$ with 5/6-filled band structure shows the metallic behavior down to 40 K.

AsF$_6$ salt are originated from the thermal excitation beyond the Mott insulating gap. These temperature dependences move parallel to the low resistivity from X = SbF$_6$, AsF$_6$, to PF$_6$, indicating the chemical pressure effect. On the other hand, β"-(C6DTP-TTF)$_3$GaCl$_4$ with the 5/6-filled band structure shows the metallic behavior down to 40 K.

References

[1] H. Urayama-Mori, H. Yamochi, G. Saito, K. Nozawa, T. Sugano, M. Kinoshita, S. Sato, K. Oshima, A. Kawamoto, and J. Tanaka, Chem. Lett., 1988, 55.
[2] H. Suzuki, K. Yamashita, M. Suto, T. Maejima, S. Kimura, H. Mori, Y. Nishio, K. Kajita, and H. Moriyama, Synthetic Metals, **144**, 89 (2004).

Authors

S. Kimura, K, Yamashita, S. Ichikawa, H. Suzuki, Y. Nishio[a], K. Kajita[a], and H. Mori,
[a]Toho Univ.

Novel Magnetoresistance Behaviors Observed in Pr$_{0.5}$Ba$_{0.5}$MnO$_3$

Y. Ueda

Recently we successfully synthesized the *A*-site ordered Ba-based manganite, *R*BaMn$_2$O$_6$ (*R* = Y and rare earth elements). The electronic phase diagram was reported as a highlight of Activity Report 2002. Compared with the *A*-site disordered R$_{0.5}$A$_{0.5}$MnO$_3$ (A = Sr, Ca), *R*BaMn$_2$O$_6$ displays remarkable features: (1) relatively high charge and orbital order (CO) transition temperatures (T_{CO}) far above 300 K, (2) a new stacking variation of the CE-type CO with a 4-fold periodicity along the *c*-axis (4CE-CO), (3) the presence of structural transition above T_{CO}, possibly accompanied by the d_{x2-y2} type orbital order, and (5) the electronic phase segregation in the end member LaBaMn$_2$O$_6$.

The discovery of such novel structural and physical properties in the *A*-site ordered manganite *R*BaMn$_2$O$_6$ has demanded new comprehension about perovskite manganese oxides. The *A*-site disordered form ($R_{0.5}$Ba$_{0.5}$)MnO$_3$ with the same constituent elements is crucial to deepen the understanding of the structural and physical properties of perovskite manganites. Very recently the *A*-site disordered Ba-based manganite $R_{0.5}$Ba$_{0.5}$MnO$_3$ has been synthesized and investigated in its structures and electromagnetic properties. The disordered form $R_{0.5}$Ba$_{0.5}$MnO$_3$ has a primitive cubic perovskite cell with no tilt of MnO$_6$ octahedra; nevertheless magnetic glassy states instead of the electronic states characteristic of perovskite manganites dominate the ground state of $R_{0.5}$Ba$_{0.5}$MnO$_3$. The magnetic glassy states could be due to the disorder effect that hinders the long-range magnetic ordering. Since the ionic radius of Ba^{2+} is much larger than that of Sr^{2+} and also R^{3+}, $R_{0.5}$Ba$_{0.5}$MnO$_3$ must include a spatial heterogeneity on a nanometer scale, which leads to the magnetic nonhomogeneous state.

Novel magnetoresistance behaviors, as shown in Fig. 1, have been observed in Pr$_{0.5}$Ba$_{0.5}$MnO$_3$. The resistivity decreases stepwise as the magnetic field increases, while the magnetization increases stepwise with the close relation to the resistivity behaviors. These behaviors are not reversible in the magnetic field. The stepwise behaviors in the magnetization and resistivity were observed up to 4.9 K but they vanished dramatically at 5.0 K. Similar behaviors were previously reported in Pr$_{0.5}$Ca$_{0.5}$MnO$_3$ doped with a few percent of other cations such as Sc, Ga or Co on the Mn site. This is the first observation of ultrasharp magnetization and resistivity change in the nondoped system. A model based on ordinal two-phase mixture cannot explain the behaviors. We have no explanation for such multi-step magnetization and resistivity change at present. However we would like to emphasize a close relation between the observed behaviors and any spatial heterogeneity on a nanometer scale.

Principal publication and authors

Y. Ueda and T. Nakajima, J. Phys.: Condens. Matter, **16** 1 (2004).

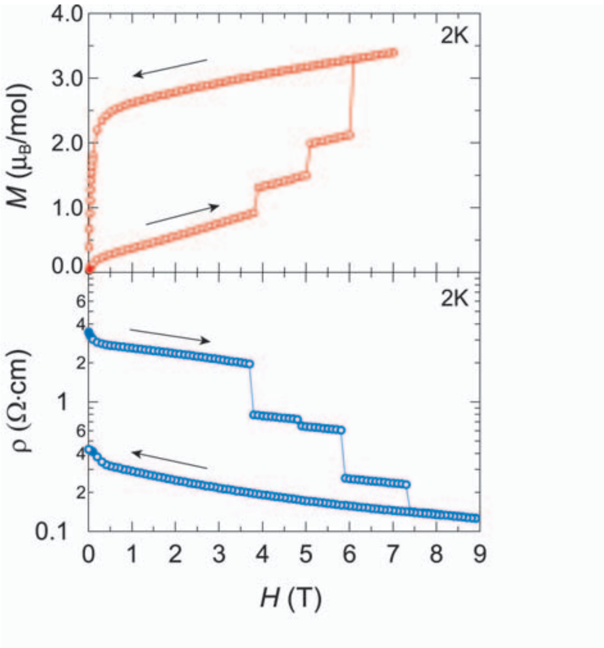

Fig. 1. Magnetic field dependence of magnetization and resistivity at 2 K in Pr$_{0.5}$Ba$_{0.5}$MnO$_3$.

The Second Example of Pressure-Induced Superconductivity in β-Vanadium Bronzes

Y. Ueda

Previously we reported the first observation of superconductivity in vanadium oxides as a highlight of Activity Report 2001. The compound is β-$Na_{0.33}V_2O_5$ which is a member of β-vanadium bronze family with the chemical formula of β-$A_xV_2O_5$ (the stoichiometric composition x = 1/3 or 0.33). There are six compounds in the family, as listed in Table 1. The monoclinic crystal structure consists of a characteristic V_2O_5-framework and A-cations. The V_2O_5-framework is formed by sharing the corners and edges of $(V1)O_6$, $(V2)O_6$ and $(V3)O_5$ polyhedra, where V1, V2 and V3 are the three crystallographically independent vanadium atoms. The $(V1)O_6$, $(V2)O_6$ and $(V3)O_5$ polyhedra form three kinds of infinite chain along the b-axis; zigzag chains, two-leg ladder chains and zigzag chains, respectively. The A-cations are located in the tunnels surrounded by the three kinds of chain. The β-vanadium bronzes show a quasi-1D conductivity along the b-axis. All members except β-$Pb_{1/3}V_2O_5$ undergo metal-insulator transitions accompanied by the charge ordering. The ground states of the low-temperature insulator phases are antiferromagnetic ordered states in β-$A^{+}_{1/3}V_2O_5$ (A^{+} = Li, Na and Ag) and spin gap states in β-$A^{2+}_{1/3}V_2O_5$ (A^{2+} = Ca and Sr). These properties are summarized in Table 1.

It is very interesting what happens when the charge order melts under high pressure. Since the discovery of the pressure-induced superconductivity in β-$Na_{1/3}V_2O_5$ we have studied the presence/absence of superconductivity under high pressure in β-vanadium bronze family. In β-$A^{2+}_{1/3}V_2O_5$, the metal-insulator transitions (charge order transitions) are suppressed under high pressure but no superconductivity has been observed at least down to 2 K. Recently we observed the superconductivity in β-$Ag_{1/3}V_2O_5$. The charge ordered phase is suppressed with increasing pressure and superconductivity appears around 7 GPa. The superconducting phase (S.C.) adjoins the charge ordered phase (C.O.) with the coexistence region of the two phases, as shown in Fig. 1. This means the first order transition from the charge ordered phase to the superconducting phase, although the nature of charge order transition on temperature seems to be a second order under ambient pressure. The supreconducting transition temperature about 6 K for β-$Ag_{1/3}V_2O_5$ is somewhat lower than 8 K for β-$Na_{1/3}V_2O_5$. The presence/absence of superconductivity in β-$A^{+}_{1/3}V_2O_5$/β-$A^{2+}_{1/3}V_2O_5$ suggests the optimum doping level of V^{4+}/V^{5+} = 1/5 for the superconductivity in β-vanadium bronze family. Very recently we have observed a sign of superconductivity with a possible T_C = 24 K in β-$Li_{1/3}V_2O_5$. A detailed experiment is now in progress.

Table 1. β-Vanadium bronze family

Compounds	V-valence	$T_{M\text{-}I}$ (K)	Ground state	Ground state (HP-ex.)
β-$Li_{1/3}V_2O_5$	$V^{4+}+5V^{5+}$	200	AFI (T_N =7 K)	SC (T_C = 24 K ?)
β-$Na_{1/3}V_2O_5$	$V^{4+}+5V^{5+}$	135	AFI (T_N = 24 K)	SC (T_C = 8 K)
β-$Ag_{1/3}V_2O_5$	$V^{4+}+5V^{5+}$	90	AFI (T_N = 24 K)	SC (T_C = 6 K)
β-$Ca_{1/3}V_2O_5$	$2V^{4+}+4V^{5+}$	150	Spin gap	PM (nonsuper)
β-$Sr_{1/3}V_2O_5$	$2V^{4+}+4V^{5+}$	170	Spin gap	PM (nonsuper)
β-$Pb_{1/3}V_2O_5$	$2V^{4+}+4V^{5+}$	-	PM	PM (nonsuper)

$T_{M\text{-}I}$: metal-insulator transition temperature
AFI : antiferromagnetic insulator
T_N : antiferromagnetic transition temperature
PM : paramagnetic metal
SC : superconductivity
T_C : superconducting transition temperature

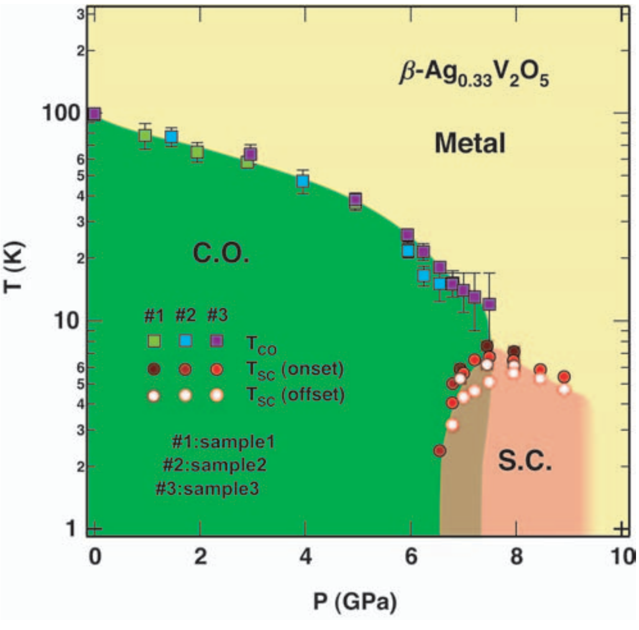

Fig. 1. The pressure-temperature (P-T) phase diagram of β-$Ag_{1/3}V_2O_5$. T_{CO} (squares) charge-ordering temperature, T_{SC} (circles) superconducting transition temperature.

Instability of the Spin-Glass Phase in a Static Magnetic Field

H. Takayama

The subject titled has been one of the fundamental issues which has remained unsettled yet in spite of extensive debates since the early stage of the spin-glass (SG) study. The mean-field theory predicts its stability up to a certain critical magnitude of a field h, while by the droplet theory the SG phase is unstable even in an infinitesimal h. Its difficulty is considered to lie on the following fact: spin dynamics governed by thermally-activated processes is so slow that even in the time-window of real experiments, we cannot distinguish whether a SG-state we are observing is in an asymptotic regime close to equilibrium or far from it. In such circumstances, a possible strategy is to perform a literal numerical experiment on nonequilibrium dynamics of model spin glasses and to compare the results with real experiments.

Following this strategy, we have examined the field-shift aging protocol on the 3D Ising Edwards-Anderson model by means of the standard Monte Carlo simulation[1,2]. In the protocol, a system is quenched to a temperature T below the transition temperature T_c ($\simeq$ 0.95 in unit of the variance of interactions), it is aged in zero field by a period of t_w, and then h is switched on and the induced magnetization $M(t)$ is

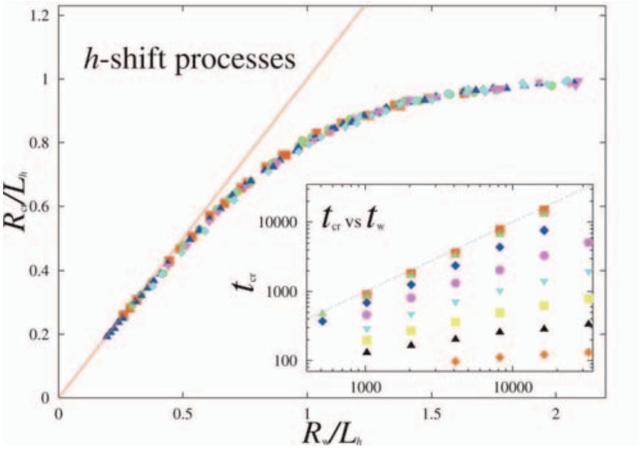

Fig. 1. Scaling plots of $R_{cr}L_h$ vs R_w/L_h of the h-shift processes at T=0.4,0.5,0.6 and 0.8. The line represents $y=x$. In the inset we plot t_{cr} vs. t_w in the h-shift processes at T=0.6 with h=0.05, 0.1, 0.2, 0.3, 0.4, 0.5, 0.6, and 0.75 from top to bottom.

measured. The system is expected to crossover from the h=0 aging state to the h>0 one around $t=t_{cr}$ which is specified by a peak position of the logarithmic time-derivative of $M(t)$. The sets of (t_{cr},t_w) for various values of h thus obtained at T=0.6 are shown in the inset of Fig. 1.

Associated with t_w and t_{cr}, we introduce the two characteristic length scales: $R_w \equiv b_T t_w^{1/z(T)}$, which is the mean size of SG domains grown in h=0 up to the field shift, and $R_{cr} \equiv b_T t_{cr}^{1/z(T) - a_T h^2}$, which is the one grown under the new field h (>0) by a period of t_{cr} after the shift. The two lengths are then scaled by the so-called field overlap length L_h. It is a key quantity in analyzing the field effect on the SG phase by the droplet theory; droplet excitations of a size L with L> (<) L_h are governed by the Zeeman (SG stiffness) energy. Surprisingly it is found that, with a proper choice of the values of a_T, b_T and $z(T)$ in the above expressions, the scaled plots of R_{cr}/L_h vs R_w/L_h of all the data obtained for different T, t_w and h lie on a single curve as shown in Fig. 1.

The consequence of the obtained scaling is clear; the h-shift aging process is nothing but a dynamical crossover from the SG state in h=0 to the paramagnetic state in h>0, or, the SG phase is unstable under h>0 in the equilibrium limit. Furthermore, when the simulated results are simply extended to the time window of the experiment on a real Ising spin glass $Fe_{0.5}Mn_{0.5}TiO_3$, our picture of the dynamical crossover turns out to be consistent with the experimental data of the occurrence of irreversibility seen by the deviation the field-cooled magnetization (FCM) from the zero-FCM, though they were interpreted before as an evidence of the AT phase transition predicted by the mean-field theory [3].

References

[1] H. Takayama, J. Magn. Magn. Mater. **272-276P1** (2004) 256.
[2] H. Takayama and K. Hukushima, to appear in J. Phys. Soc. Jpn., preprint cond-mat 0307641.
[3] H. Aruga Katori and A. Ito, J. Phys. Soc. Jpn. **63** (1994) 3122.

Authors
H. takayama and K. Hukushima[a]
[a]Dept. Basic. Sci. Univ. Tokyo

New Superconducting Pyrochlore Oxides

Z. Hiroi

We have been searching for a new superconductor with a higher transition temperature T_c since the discovery of copper oxide superconductor by Bednorz and Muller in 1986. Many copper oxide superconductors have been synthesized, and the world record of T_c reached 135 K at ambient pressure, which was reported in the mercury containing copper oxide in 1993. After 10 years, it becomes more and more difficult to find a new copper oxide superconductor even with low T_c's. The playground of these superconductors is a CuO_2 sheet which consists of square arrangement of Cu atoms. However, there is another class of lattices in nature made of triangles such as triangular or kagome lattice. Recently, effort to search for a new superconductor in such triangle-based lattices has been done extensively, and is already successful in the triangular lattice of CoO_2 in $Na_xCoO_2 \cdot yH_2O$ with T_c = 5 K by Takada [1] and in the three-dimensional pyrochlore lattice made of tetrahedra in $Cd_2Re_2O_7$ with T_c = 1 K by our group [2]. Although the T_c is rather low, the mechanism of superconductivity seems very interesting on the basis of uniqueness of the triangle-based lattices. In 2003 we discovered a new family of pyrochlore oxides AOs_2O_6 called the β-pyrochlore oxide which shows superconductivity with T_c up to 10 K [3], ten times higher than in the α-pyrochlore oxide $Cd_2Re_2O_7$.

The α-pyrochlore oxide has the general chemical formula $A_2B_2O_7$ or $A_2B_2O_6O'$, where A is a larger cation and B is a smaller transition metal (TM) cation. The ideal structure is composed of two types of cation-oxygen sublattice: one is a corner-sharing tetrahedral network composed of A atoms with an O' atom in the center of each tetrahedron, and the other is that of B atoms with each B atom coordinated quasi-octahedrally by six O atoms. This type of tetrahedral network is called the pyrochlore lattice, and has been studied extensively in order to elucidate the effect of geometrical frustration on the properties of localized spin and itinerant electron systems. In contrast, the β-pyrochlore oxide has the general chemical formula AB_2O_6 and crystallizes in a similar cubic structure with space group $Fd\bar{3}m$ as in the α-pyrochlore oxide, but with a large, monovalent alkaline metal ion located at the O' site of the α-pyrochlore structure, as shown in Fig. 1. This means that the A_2O' unit of the α-pyrochlore is replaced by a large A atom in the β-pyrochlore. We synthesized three β-pyrochlore osmates for A = K [3], Rb [4], and Cs [5].

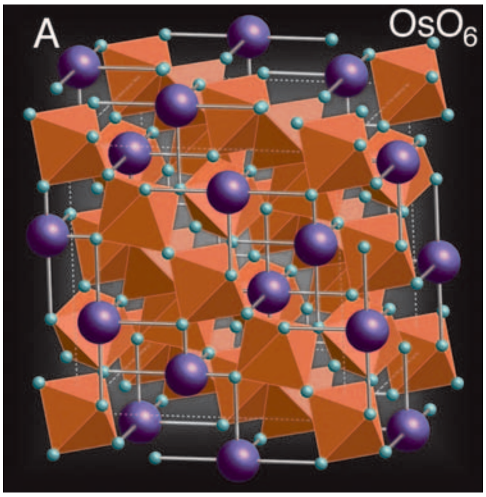

Fig. 1. Structural view of the β-pyrochlore oxide AOs_2O_6. The red octahedron with six light blue balls on the vertices represents the OsO_6 unit, and the big ball does an A atom that is coordinated by six oxygen atoms from surrounding OsO_6 octahedra. The crystallographic sites are $8b$, $16c$ and $48f$ in the space group Fd-$3m$ for A, Os and O atoms, respectively. The pyrochlore lattice emerges from the structure by extracting only osmium atoms.

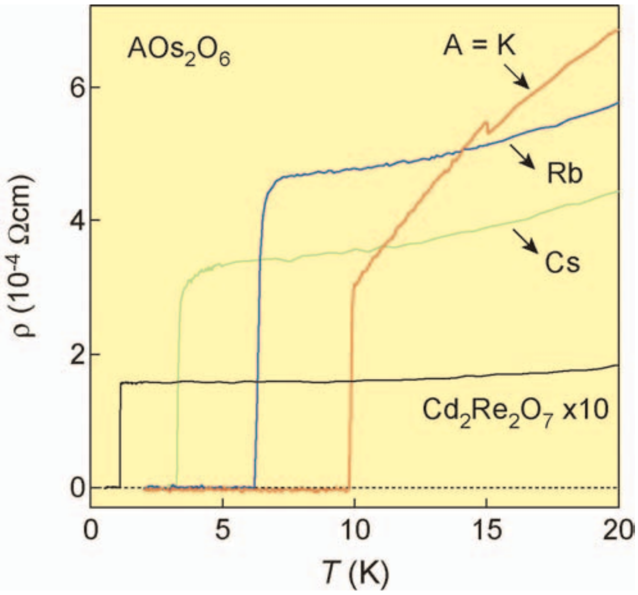

Fig. 2. Temperature dependence of resistivity (ρ), showing a superconducting transition at T_c = 9.6 K, 6.3 K, and 3.3 K for three β-pyrochlore oxides with A = K, Rb, and Cs, respectively. That of α-pyrochlore oxide $Cd_2Re_2O_7$ with T_c = 1.0 K is also shown, after multiplied by 10.

Figure 2 shows the temperature dependence of resistivity measured on polycrystalline samples. The T_c is 9.6 K, 6.3 K, and 3.3K for A = K, Rb, and Cs, respectively. As the lattice is expanded with increasing the ionic radius of the A ions from K^+ to Cs^+, the T_c decreases gradually. This suggests that the T_c decreases with imposing negative chemical pressure upon the Os pyrochlore lattice, which is in contrast to the case of conventional BCS superconductor where the T_c may increase under negative pressure with increasing the density-of-state at the Fermi level. The mechanism of superconductivity in the β-pyrochlore oxides is not known at the moment, but we believe that interesting physics is involved there on the triangle-based lattice.

References

[1] K. Takada, *et al*., Nature **422**, 53 (2003).
[2] M. Hanawa, *et al*., Phys. Rev. Lett. **87**, 187001 (2001).
[3] S. Yonezawa, *et al*., J. Phys.: Condens. Matter **16**, L9 (2004).
[4] S. Yonezawa, *et al*., J. Phys. Soc. Jpn. **73**, 819 (2004).
[5] S. Yonezawa, *et al*., J. Phys. Soc. Jpn., in press.

Authors

S. Yonezawa, Y. Muraoka, and Z. Hiroi

Superconducting Network with Magnetic Decoration --- Hofstadter Butterfly in Spatially Modulated Magnetic Field

Y. Iye

Energy spectrum of tight-binding electrons on a two-dimensional (2D) square lattice under a magnetic field perpendicular to the plane has an exquisite structure, known as Hofstadter butterfly. Experimental verification of the full Hofstadter butterfly spectra is a formidable task, although recent attempts using semiconductor lateral superlattice seem to attain a certain degree of success. Superconducting wire network constitutes an experimental system intimately related to the Hofstadter problem. It has been demonstrated that the Little-Parks oscillation a superconducting wire network exhibits fine structures at commensurate values of α (average flux per plaquette), and that $\Delta T_c(H)$ reproduces the edge shape of the Hofstadter spectrum for the corresponding 2D lattice. These and the majority of subsequent studies were conducted in a uniform magnetic field. In the present

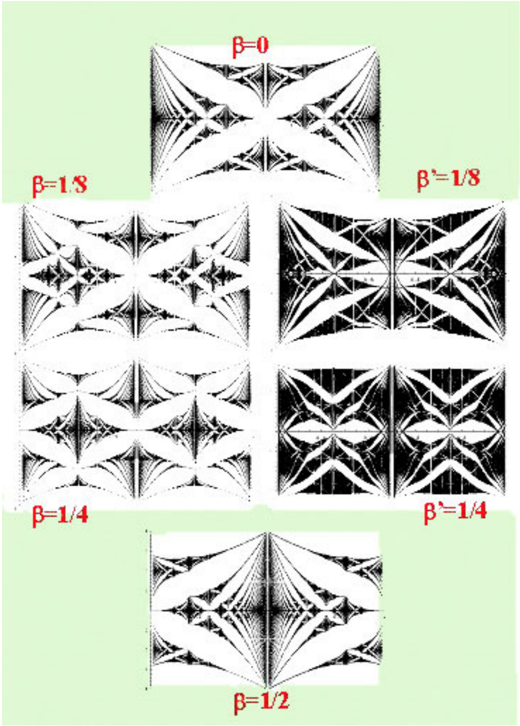

Fig. 1. Hofstadter butterfly spectra under spatially modulated magnetic field of checkerboard (*left*) and stripe (*right*) patterns.

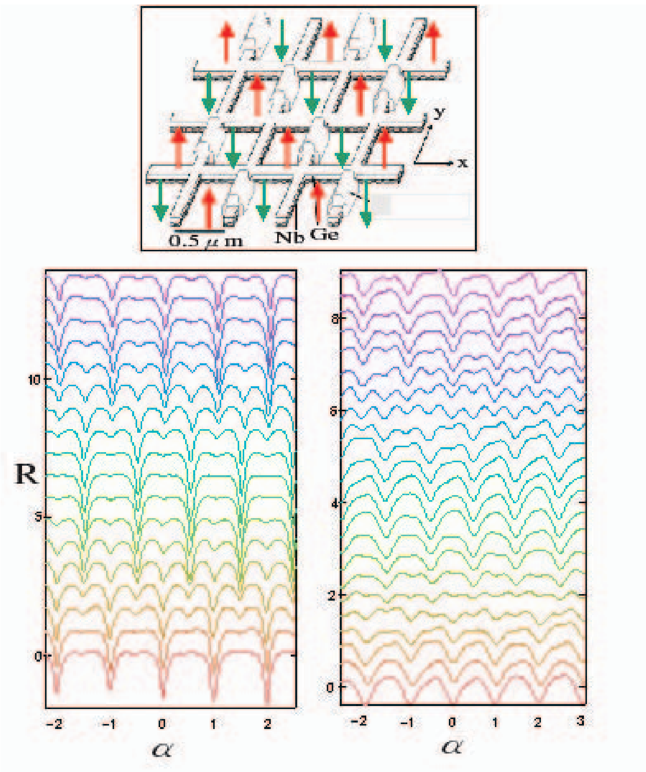

Fig. 2. (*Top*) Superconducting network decorated with a ferromagnetic array. Experimental traces of Little-Parks oscillation for the checkerboard (*left*) and stripe (*right*)

study, we address ourselves to the case of spatially varying magnetic field,.

Figure 1 shows the evolution of the Hofstadter spectra in the presence of a spatially alternating external flux pattern, whose amplitude is denoted by the parameter β. The spectrum at the top is the original Hofstadter butterfly corresponding to β=0. The route on the left side is for a checkerboard pattern, and that on the right side is for a stripe pattern. The spectra for the two cases become identical again for β=1/2,

The corresponding experimental system was realized by use of mesoscopic superconductor/ferromagnet hybrid structures. Typical structure is shown in Fig. 2. A superconducting wire network is decorated by a ferromagnetic array. The latter is magnetized by an external magnetic field applied parallel to the network plane. The stray magnetic field generated by the ferromagnetic array creates a checkerboard-pattern flux arrangement. The amplitude of the spatially varying field can be continuously varied by changing the azimuthal angle of the parallel field.

The lower left panel of Fig. 2 shows the Little-Parks oscillation as a function of perpendicular magnetic field for the checkerboard field. With increasing amplitude of the checkerboard field, the dips at half-integer flux develop, and take over those at integer flux. At a higher value of the checkerboard field, the original oscillation pattern is restored, and the cycle is repeated. The lower right panel shows the corresponding date for a stripe field.
A conspicuous difference from the checkerboard case is that the oscillation amplitude becomes much reduced at β=1/4. This and other features are in line with the behavior of the spectral edge shown in Fig. 1.

Authors
Y. Iye, E. Kuramochi, M. Hara, A. Endo, and S. Katsumoto

Non-Democratic Nature of Wavefunctions in Quantum Dots

S. Katsumoto

In an elementary course of quantum mechanics, students learn that the parity of wavefunction in a quantum well changes alternatively with the energy eigenvalue. However in the transport through semiconductor quantum dots, it was found that long trains of in-phase resonant peaks appear, in other words, many neighboring states have the same parity, which has been a long standing problem in the transport through quantum dots [1].

We have clarified that this is due to a non-democratic nature of wavefunctions in quantum dots, *i.e.*, there exist some special states with anomalously strong couplings with the electrodes, which dominate the parity of surrounding ordinal states.

The existence of such strongly coupled states (SCSs) can be known from the interference between an ordinal resonant tunneling path and a path through an SCS by co-tunneling. The interference results in a characteristic lineshape of the resonant peaks, known as the Fano effect [2].

Figure 1(a) shows the conductance around zero-bias versus the gate voltage. In order to magnify the effect of SCSs, the dot is in a region of parameters between Coulomb blockade and open dot. Coulomb resonant "dips" appear instead of ordinal peaks. This is because the conductance of the co-tunneling path is so high that the opening of the resonant path causes negative interference and results in decrease in the total conductance. This is also confirmed by the fact that the Coulomb diamonds appear as high conductance regions as shown in Fig. 1(b). As indicated by solid curves, every dip has the Fano-type distortion.

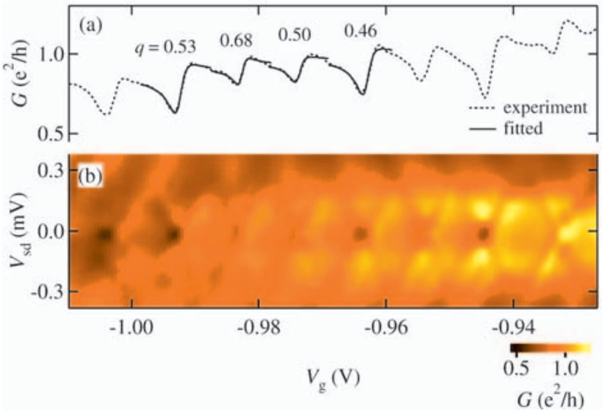

Fig. 1. (a) Coulomb resonant "dips" appeared in the transport through a quantum dot, which is in between a Coulomb blockade and an open dot. Sold curves are the results of fitting by Fano formula. (b) "Reversed" Coulomb diamonds appeared in a color plot of the conductance against the plane of source-drain bias and gate voltage.

What is the origin of such non-democratic social structure in quantum dots? It is known that in some energy region in non-integrable potential, wavefunction "scarring" occurs, in which the probability amplitude is high along corresponding classical trajectory. If such "scar" connects the inlet and the outlet of the dot, the transmission coefficient through the level is very high producing an SCS.

Then the magnetic field applied perpendicular to the dot causes Lorentz bending of the scarred trajectory and focusing of other scarred wavefunction, hence series of transitions occurs. Figure 2 shows such properties in the ridges of conductance. When the field is low and the cyclotron diameter is larger than the dot size, the transitions of the ridges are

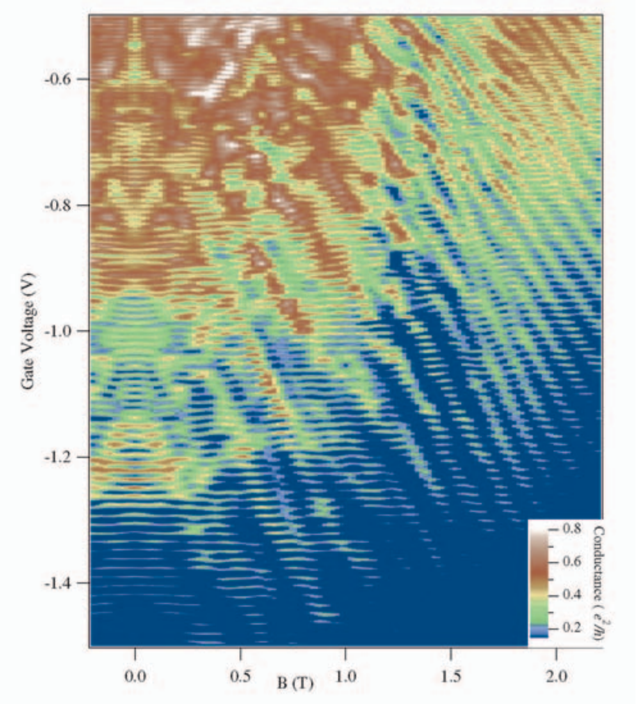

Fig. 2 Color plot of the conductance of a quantum dot versus the plane of the gate voltage and the magnetic field. Small oscillation along the gate voltage is the Coulomb oscillation.

significantly disordered. On the other hand, at high fields, the shrinkage of the cyclotron motion leads to the formation of edge states, and the transitions become quite regular, where the SCS is the edge state placed closest to the electrodes.

References
[1] R. Schuster et al., Nature **385**, 417 (1997).
[2] K. Kobayashi, H. Aikawa, S. Katsumoto and Y. Iye, Phys. Rev. Lett. **88**, 256806 (2002).

Authors
S. Katsumoto, H. Aikawa, K. Kobayashi, A. Sano, and Y. Iye

Strain-dependent Dissociation of Molecules and Diffusion of Adsorbates on a Nitrogen Adsorbed Cu(001) Surface

F. Komori

Dissociative adsorption of molecules and diffusion of adsorbates on strained metal surfaces have been studied both experimentally and theoretically [1]. The observed preferential dissociation and small diffusion at the stretched surfaces are attributed to the changes in the electronic energy levels and the width of d-bands due to the lattice deformation on the basis of the density-functional calculations.

We have studied adsorption of oxygen molecules on a grid pattern of the partly nitrogen-covered Cu(001) surface at room temperature (RT) by scanning tunneling microscopy (STM) [2]. On this surface, nitrogen-adsorbed patches with average size of 5×5 nm^2 are regularly arranged on clean Cu surface. The Cu-N short-range attractive interaction makes the local c(2×2)N structure while the nanometer-scale grid pattern is caused by the minimization of the total elastic energy including the substrate. The Cu lattice at the patch is stretched by the adsorption while that at the clean surface is inhomogeneously compressed up to 5 %. The STM image shown in Fig. 1 demonstrates the lattice distortions at both clean Cu surface and the nitrogen-adsorbed patch near the boundary.

Oxygen molecules are dissociatively adsorbed on the clean Cu(001) surface of the grid pattern without changing the nitrogen-adsorbed surface. The adsorbate density is small on the narrow surface where the Cu lattice is highly compressed, indicating the strain-dependent dissociation probability. Especially, there are few adsorbates at the intersections of the Cu grid connected only to the narrowest Cu lines. The oxygen adsorbate can migrate on the clean surface at RT except on the narrowest lines. The adsorbates on narrow areas diffuse more rapidly than on wide areas as shown in Fig.2. On a connected broad Cu area of the grid the more oxygen adsorbates are seen on the wider region where the lattice is less compressed. The diffusion barrier of the oxygen adsorbates is smaller at the more compressed surface area on the Cu grid. These results are consistent with the predictions by the *d*-band model that the dissociation probability of oxygen molecule and the diffusion barrier of the oxygen adsorbates are small on the highly compressed area.

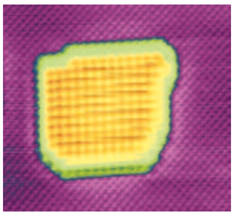

Fig. 1. An STM image showing a c(2×2)N patch (red-yellow) surrounded by (1×1) Cu surface (purple). The protrusions of the Cu atoms on the clean Cu surface are enhanced separately from those of the nitrogen atoms inside the c(2×2)N patch. The latter at the hollow site of the Cu lattice is imaged yellow. The average coverage of nitrogen on this surface is 0.1 ML. The size of the image is 11.9 × 11.1 nm^2.

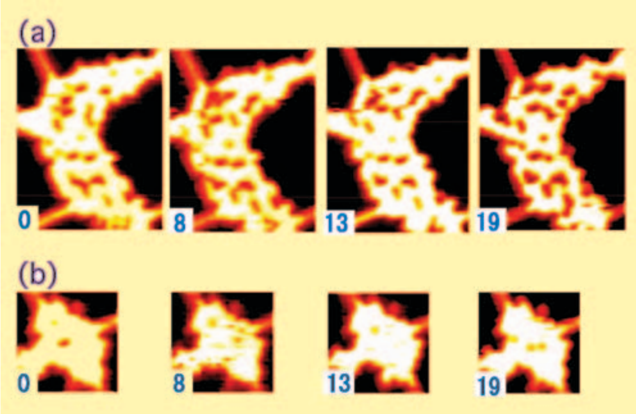

Fig. 2. Successive STM images for (a) wide and (b) narrow areas on the clean Cu surface of the nitrogen modified grid pattern after oxygen molecule adsorption. The latter area is connected only to the narrowest clean Cu lines. Black areas are nitrogen-adsorbed surface. Yellow dots are oxygen atoms adsorbed on the clean Cu surface. The numbers at the left-bottom corners show the times (minutes) after the scanning of the surface started. The image sizes are (a) 8.0 × 10.4 nm^2, and (b) 5.6 × 5.6 nm^2 .

References
[1] for example, M. Gsell, P. Jakob and D. Menzel, Science **280** (1998) 717.
[2] S. Ohno, K. Yagyuu, K. Nakatsuji and F. Komori, Surf. Sci. **554** (2004) 183.

Authors
S. Ohno, K. Yagyuu, K. Nakatsuji, and F. Komori

Lateral Displacement by Transient Mobility in Chemisorption of CO on Pt(997)

J. Yoshinobu

When a gaseous molecule enters in a chemisorption potential well and chemisorbs on the surface, the adsorption energy has to be dissipated. This energy is transferred to not only various motions of the molecule on the surface but also electron-hole pair and phonon excitations of the substrate. A "hot precursor" species in such energy dissipation processes is transiently mobile on the surface, which plays an important role not only in thin film growth, surface chemical reaction but also molecular manipulation of adsorbates. However, the lateral displacement by the transient mobility of an incoming molecule has not been accurately determined yet. In this study [1], the adsorbed states of CO on Pt(997) at 11K have been investigated by means of infrared reflection absorption spectroscopy (IRAS). At 11K thermal migration is suppressed and thus the initial chemisorption at terrace sites and step sites is controlled by the transient mobility of

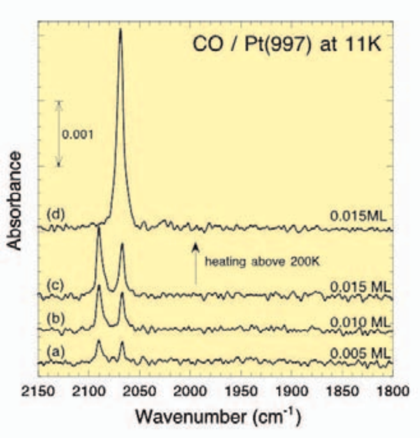

Fig. 1. A series of IRAS spectra of CO on Pt(997) at 11K. (a) 0.005ML, (b) 0.010ML and (c) 0.015ML. (d) After heating the 0.015ML CO adsorbed surface above 200K and cooled to 11K.

adsorbing molecule.

Figures 1(a)-(c) show a series of IRAS spectra for adsorbed CO on Pt(997) at 11K. Two peaks are clearly observed at 2067 cm^{-1} and 2090 cm^{-1}, and they are ascribed to atop CO at step and atop CO at terrace, respectively. With increasing the coverage from 0.005, 0.010 to 0.015 ML (monolayer), two peaks do not shift, and the integrated absorbance of each peak is proportionally increased. These experimental results indicate that adsorbed CO species do not interact each other, i.e., they are singleton CO species. By heating the adsorbed surface, thermal migration is activated and all CO species are chemisorbed at step sites (Fig. 1(d)). Since CO does not desorb by 200K heating, all CO species become adsorbed at step sites. From these results, the initial occupation ratio between atop CO at terrace and atop CO at step is directly estimated to be 3.6:1.

In order to estimate the lateral displacement of transient mobility for CO on Pt(997), we introduce a simple model which includes following assumptions (see Fig. 2). (1) Gaseous CO molecules uniformly collide with the surface. (2) The transient migration occurs randomly on Pt(997). (3) Once CO moves across a step during the transient migration, it sticks at a nearby atop site on the step and never moves anymore. (4) The initial kinetic energy of gaseous CO is neglected since it is very small as compared with the adsorption energy (~1.3eV) and the diffusion barrier (0.19 eV). Using this simple model, the occupation probability at step sites, P(step), is easily calculated to be $2l/\pi L$, where L is the distance between steps. In the present experiment, P(step) =1 /(3.6+1)=0.217 and L = 2.0nm, we can estimate the lateral displacement of transient mobility for CO on Pt(997) to be 0.68nm.

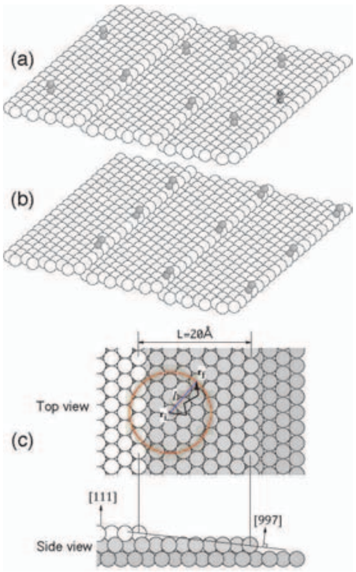

Fig. 2. (a) Schematic model of adsorbed CO on Pt(997) at 11K and (b) that after heating above 200K (~0.016ML). (c) An isotropic migration model. r_i: the first impact point. r_f: the initial chemisorption site. l: the mean lateral displacement of the transient mobility.

Reference

[1] J. Yoshinobu, N. Tsukahara, F. Yasui, K. Mukai and Y. Yamashita, Phys. Rev. Lett. **90** (2003) 248301.

Authors

J. Yoshinobu, N. Tsukahara, F. Yasui, K. Mukai, and Y. Yamashita

Kondo Transport Studied by the Finite Temperature Density Matrixrenormalization Group Method

K. Ueda

Transport properties through quantum dots have been of great interest in recent years. At high temperatures the conductance through a dot shows peaks as a function of the gate voltage when the number of electrons in the dot changes, which are known as Coulomb oscillation peaks. When the number of electrons is odd, the conductance becomes larger as temperature is lowered below a characteristic temperature and reaches to the unitarity limit ($2e^2/h$) in the low temperature limit. This effect of Kondo transport was actually observed a few years ago [1]. One of the interesting features of the Kondo transport compared with the usual Kondo effect of a magnetic impurity in a metal is that various parameters are tunable in quantum dots. A typical example is that the number of electrons in the quantum dot is easily-varied by changing the gate voltage.

Recently we have developed a numerical scheme to calculate the conductance through a quantum dot by using the finite temperature density matrix renormalization group (FT-DMRG) method [2]. A minimal model for the transport thorough a quantum dot is the one dimensional tight binding model with an impurity site in the middle.

$$\begin{aligned} H \; &:= -\sum_{i\sigma} t_{i,\,i+1}\;(c^\dagger_{i\sigma}c_{i+1\sigma} + \text{h.c.}) \\ &\quad + \epsilon_d \sum_{\sigma} c^\dagger_{0\sigma}c_{0\sigma} + U c^\dagger_{0\uparrow}\,c_{0\uparrow}\,c^\dagger_{0\downarrow}\,c_{0\downarrow} \qquad (1) \end{aligned}$$

$$t_{i,\,i+1} \;:= \begin{cases} v & \text{when } \; i = 0, \;\; i+1 = 0, \\ t = 1 & \qquad \text{others,} \end{cases} \qquad (2)$$

where ϵ_d is the energy level of the state in the dot and U is the Coulomb interaction when two electrons are put into the dot. The energy level ϵ_d may be varied by changing the gate voltage. The coupling constant between the dot and the leads is given by v.

Conductance through the dot is expressed by the Green function at the impurity site, $G_0\,(\omega)$. The Green function in the frequency space can be calculated by the analytic continuation from the thermal Green function as a function of the imaginary time, $G_0\;(\tau)$ obtained by FT-DMRG. The

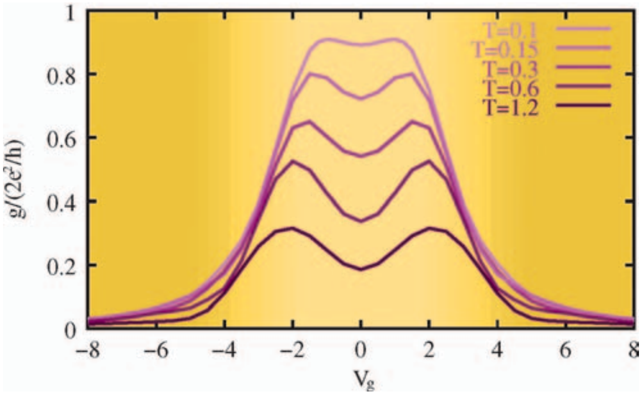

Fig. 1. Conductance $g/(2e^2/h)$ as a function of the gate voltage V_g for $v = t/\sqrt{2}$ and U=4t at various temperatures calculated by the FT-DMRG.

numerical analytic continuation generates a main error of $G_0(\omega)$, but its integrated value like the conductance shows a better behavior than $G_0(\omega)$ itself.

Figure 1 is an example of the conductance through the quantum dot as afunction of the gate voltage which is defined by $\epsilon_d = -U/2 + V_g$. One can see the crossover from the Coulomb oscillation behavior at high temperatures to the Kondo resonance below the Kondo temperature.

An advantage of the FT-DMRG is that once the eigen vectors for the bulk part is obtained the Greens function at the impurity site can be calculated simultaneously for various impurity parameters like the gate voltage. In this sense, the FT-DMRG is a very convenient and powerful tool to discuss transport properties through quantum dots when the Kondo temperature is not so small.

References

[1] W. G. van der Wiel, et. al.: Science **289** (2000) 2105.
[2] X. Wang and T. Xiang: Phys. Rev. B **56** (1997) 5061; N. Shibata: J. Phys. Soc. Jpn. **66** (1997) 2221.

Authors

I. Maruyama, N. Shibata[a], and K. Ueda
[a] Dept. of Basic Science, Univ. of Tokyo.

A Unified Approach to Filling- and Bandwidth-Control Mott Transitions

M. Imada

The nature of the system in which quantum fluctuations and electron correlations play essential roles is one of the main subjects in condensed matter physics. When the kinetic energy and the Coulomb repulsion compete severely, the ground state of many-body electron systems can be highly nontrivial. Metal-insulator transitions driven by the electron correlation postulated by Mott [1] provide a typical example of such a nontrivial behavior.

In the transition to the Mott insulator, it is known that there exist two different basic routes to control the competition of the interaction and kinetic energies. One is the control by bandwidth (relative to Coulomb repulsion) and the other is filling (averaged number of carrier electrons in a unit cell). Controls by these two parameters can be found in a lot of examples in real materials including transition metal compound, organic materials and ^{3}He systems. In spite of plenty of the experimental results, phase diagrams of the Mott insulator and metals have not been fully elucidated in microscopic theoretical descriptions.

The Hubbard model with nearest- and next-nearest-neighbor transfers is a minimal model to describe the essence of the Mott insulator and metals with their transitions on the bandwidth- and filling-control routes. The filling-control Mott transition (FCMT) was studied at zero temperature by the quantum Monte Carlo method in the Hubbard model on a square lattice [2]. The transition shows a continuous character with a singular divergence of the compressibility and critical divergence of the antiferromagnetic correlation length. The bandwidth-control Mott transition (BCMT) was studied also at zero temperature by the path integral renormalization group method [3]. In contrast to the FCMT, the BCMT shows a first-order transition, although a naive expectation is that the continuous FCMT anticipates also the continuous BCMT. This contrast is essentially consistent with the trend of the experimental observations cited above.

Mott has originally proposed a first-order BCMT because of the role of the long-ranged part of the Coulomb interaction [1]. However, the numerical result shows that the first-order transition takes place even with the onsite interaction only. In this circumstance, it has been greatly desired to clarify basic properties of the BCMT and the FCMT in a unified way to further elucidate the contrast.

In this study, we have developed the grand-canonical path-integral renormalization group method [4] which is useful to calculate chemical potential dependence of physical quantities. The path-integral renormalization group method has been originally developed in the canonical ensemble. This algorithm does not suffer from negative-sign problem and can be applied to any lattice structure with any boundary conditions. Extension of this algorithm to the grand-canonical framework makes it possible to study the correlated electron systems whose control parameters are filling, bandwidth and lattice structure in a unified way. In the grand-canonical path-integral renormalization group calculations, metal-insulator transitions are carefully examined with finite-size scalings and extrapolations to the thermodynamic limit.

By using the newly developed method, the ground-state phase diagram of the Hubbard model with next-nearest-neighbor transfer scaled by nearest-neighbor transfer t'/t =-0.2 on the square lattice has been determined in the plane of chemical potential μ and Coulomb interaction U [4] (Figure 1). The Mott-insulator phase is drawn as the pink area and the metallic phase is drawn as the yellow area. The remarkable result is that the V-shaped Mott insulator phase appears. At the corner of the V-shaped metal-insulator boundary, the BCMT occurs and at the edges except the corner, the FCMT occurs. We have confirmed the continuous character of the FCMT with diverging charge compressibility and the first-order BCMT with a jump of the double occupancy.

To analyze the relation between the shape of the phase boundary and the order of the metal-insulator transition, we have analytically derived a general relation of the slope of the metal-insulator transition line in the μ-U phase diagram and physical quantities [4]: In the case of the first-order metal-insulator transition, $\Delta U/\delta\mu$ is expressed by the ratio of the jumps in the filling and the double occupancy $\Delta n/\Delta D$. In the case of the continuous transition, $\Delta U/\delta\mu$ is expressed by the ratio of the compressibility and dn/dU in the metallic phase. These relations can be regarded as generalizations of Clausius-Clapeyron and Ehrenfest equations in

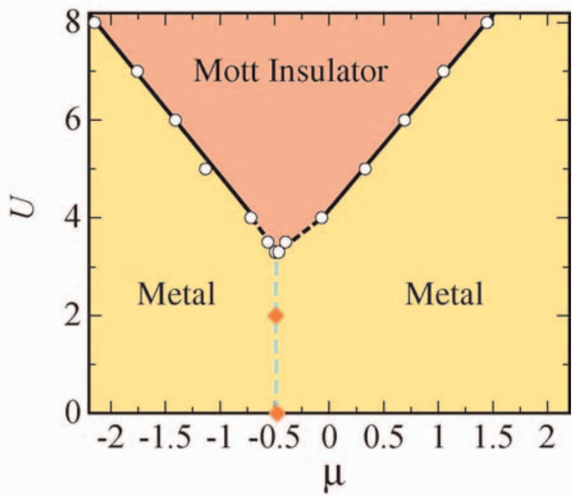

Fig. 1. Ground-state phase diagram in the plane of chemical potential μ and Coulomb interaction U for nearest-neighbor transfer t=1.0 and next-nearest-neighbor transfer t'=-0.2 on the square lattice in the thermodynamic limit [4]. Open circles represent the metal-insulator boundary extrapolated to the thermodynamic limit by using the data of N=4×4, 6×6, 8×8, 10×10 lattice systems. The solid black lines represent the least-square fit of metal-insulator boundary for U=4.0, 5.0, 6.0, 7.0 and 8.0. The V-shaped Mott insulator phase is drawn as pink area and the metallic phase is drawn as the yellow area. The corner of the V-shaped metal-insulator boundary is the bandwidth-control Mott transition point and the edges are the filling-control Mott transition points. The red diamonds represent chemical potentials for half filling for U=0.0 and U=2.0 in the thermodynamic limit. By connecting those points to the bandwidth-control Mott transition point, the blue-dashed line represents the half-filled density, which is the bandwidth-control route in the metallic phase.

the first- and second-order transitions at finite temperature, respectively, to the quantum phase transitions.

These relations support that the V-shaped phase boundary is resulted from the first-order BCMT coexisting with the continuous FCMT with diverging compressibility. Namely, it is shown that the V-shaped metal-insulator transition line together with the first-order BCMT is not compatible with the presence of the first-order FCMT near the BCMT. When the V-shaped Mott insulator phase appears, the charge gap Δ_c opens at U=U_c and shows marked linear dependence on U for U>U_c, namely, $\Delta_c \sim U-U_c$. It is noted that the linear opening of the Mott gap has been actually observed in the perovskite compounds, $R_{1-x}Ca_xTiO_3$ [5], which is consistent with our results.

We have also shown the possible and impossible shapes of the metal-insulator boundary with first-order and continuous transitions by using the thermodynamic relations derived above: The ϒ-shaped structure of the insulator phase with the first-order BCMT coexisting with the first-order FCMT can be realized in contrast with the V-shaped case. On the other hand, in the case of the U-shaped insulator phase (for example, the case with an essential singular form of the charge gap as $\Delta_c \sim \exp[at/(U-U_c)]$), if the first-order BCMT exists at the corner, the first-order transition cannot be retained at the FCMT, which is classified to the same class as the V-shaped case.

References

[1] N. F. Mott and R. Peierls: Proc. Phys. Soc. London. A **49** 72 (1937).
[2] N. Furukawa and M. Imada: J. Phys. Soc. Jpn. **61** 3331 (1992).
[3] T. Kashima and M. Imada: J. Phys. Soc. Jpn. **70** 3052 (2001).
[4] S. Watanabe and M. Imada: J. Phys. Soc. Jpn. **73** 1251 (2004).
[5] T. Katsufuji, Y. Okimoto and Y. Tokura: Phys. Rev. Lett. **75** 3497 (1995).

Authors

S. Watanabe and M. Imada

From Chemical Bonding to Confinement Due to Nonadiabatic Processes by the Enhancement of Quantum Fluctuations

Y. Takada

The physical nature of chemical bonding has been studied in the adiabatic approximation in which only electronic motion contributes to the formation of covalent bonds. Although this approximation may well apply to most realistic molecules and solids, a more comprehensive understanding of chemical bonding will be obtained by investigating the roles of quantum fluctuations of nuclei in the bond formation.

We have commenced such an investigation by considering a hydrogen-like molecule, ($M^+M^+m^-m^-$), composed of two unit-positive charge particles ('protons') with mass M and two electrons with mass m. The mass ratio m/M is changed continuously from zero (the adiabatic limit) to unity (the limit of dipositronium), covering the issue of a biexciton or a bound complex of two electrons and two holes in between. We have employed the diffusion Monte Carlo (DMC) simulations at zero temperature in order to evaluate the exact values for various ground-state properties such as the total energy E_0 and the average separation of 'protons' (or the bond length), together with the corresponding ones in the adiabatic approximation.

In Fig. 1, the calculated result for E_0 in DMC is shown as a function of m/M by the solid curve. The obtained E_0 increases monotonically with increasing m/M, but it is always smaller than the upper limit of the energy for the existence of a bound state of this four-body problem (the dotted curve), namely, $E_0 = -M/(m+M)$ in hartree units. The adiabatic approximation provides a very accurate value for E_0 with relative errors less than only 1% as long as m/M is smaller than 0.1, convincing us that the binding mechanism

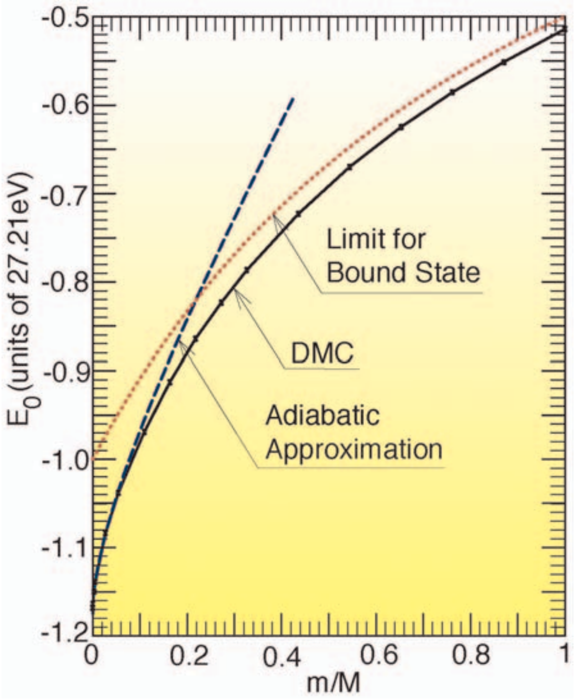

Fig. 1. Ground-state energy of a hydrogen-like molecule ($M^+M^+m^-m^-$) in both DMC and the adiabatic approximation as a function of the mass ratio m/M.

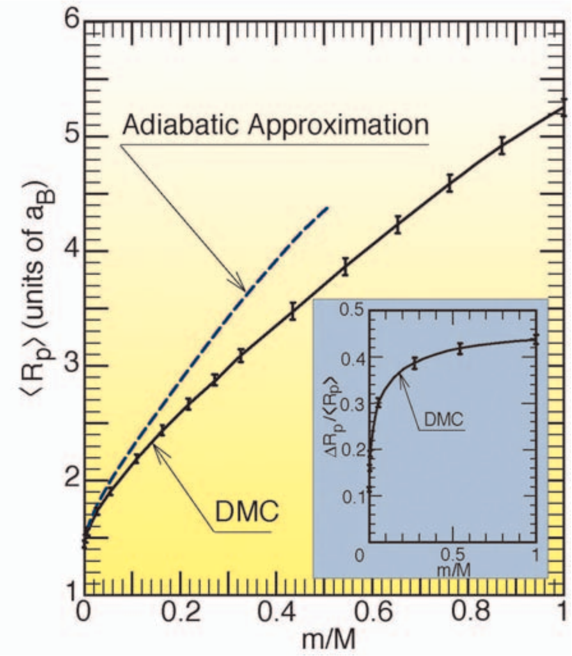

Fig. 2. Average distance between two ‘protons’ $<R_p>$ in uints of the Bohr radius as a function of m/M. The inset shows the relative variation $\Delta R_p/<R_p>$.

for this molecule in this range of *m*/*M* is nothing but the chemical bonding in the usual argument [1].

The decrease of the binding energy with increasing *m*/*M* is associated with the rapid increase of the bond length as shown in Fig. 2. Thus the vibrons or the zero-point quantum fluctuations of ‘protons’ are found to hamper this chemical bonding by weakening the binding energy and widening the bond length.

For *m*/*M* larger than about 0.2, the adiabatic approximation becomes too crude to support any bound states in the system. Concomitant with this result for E_0, the variation of ‘proton’ positions is as large as the average separation of two ‘protons’. This implies that proton motion has changed its character with the increase of *m*/*M*; at *m*/*M*<<1, ‘protons’ are localized and separated to each other by the bond length, while for *m*/*M* larger than about 0.2, they overlap in the whole molecule in just the same way as electrons.

Since the adiabatic potential cannot afford an enough attractive energy to bind ‘protons’ for *m*/*M*>0.2, the existence of a bound state (or the confinement of this four-body system) as demonstrated by DMC suggests that nonadiabatic processes or the effects due to retardation of electron response to ‘proton’ motion should play a crucial role in the binding mechanism for *m*/*M* in this region [2].

Finally we note that the parameter *m*/*M* controls the two competing effects on the binding mechanism; one is to weaken the binding force through enhancing quantum fluctuations and the other is to strengthen it through promoting nonadiabatic processes. The crossover takes place at *m*/*M* around 0.2.

References

[1] K. Ruedenberg, Rev. Mod. Phys. **34**, 326 (1962).
[2] Y. Takada and T. Cui, J. Phys. Soc. Jpn. **72**, 2671 (2003).

Authors
Y. Takada and T. Cui[a]
[a]Jilin University.

Superconductivity and Abelian Chiral Anomalies

M. Kohmoto

The importance of quantum-mechanical phases in condensed matter physics has been recognized and emphasized for recent several decades. The fundamental character of a vector potential is evident in the Aharonov-Bohm effect where the U(1) gauge structure is essential and a magnetic field in itself plays only a secondary role [1]. Topological structures in quantum gauge field theories have also been studied and extensive knowledge has been accumulated [2]. Quantum mechanics itself supplies a fundamental gauge structure [3]. It is known as geometrical phases in many different contexts, where gauge structures emerge by restricting physical spaces. The quantum Hall effect is one of the key phenomena to establish the importance of geometrical phases [4].

The topological character of the Hall conductance was first realized by the Chern number expression, where the Bloch functions define "vector potentials" in the magnetic Brillouin zone accompanied with a novel gauge structure [5]. Further the ground state of the fractional quantum Hall effect is a complex many-body state where another kind of gauge structure emerges [6].

These quantum states with nontrivial geometrical phases are characterized by topological orders which extend an idea of order parameters in statistical mechanics to the quantum states without spontaneous symmetry breaking [7].

Recently, following a prediction of flux phases for correlated electron systems, spin Hall conductance is defined for superconductors based on the Bogoliuvov-de Gennes (B-dG) equation [8].

In Ref.9, we established a topological characterization of general superconductivity based on the BdG equation on lattices. A map to a parameter space which represents the BdG hamiltonian is considered. In the parameter space, an analogue of the Dirac monopole exists and the Chern num-

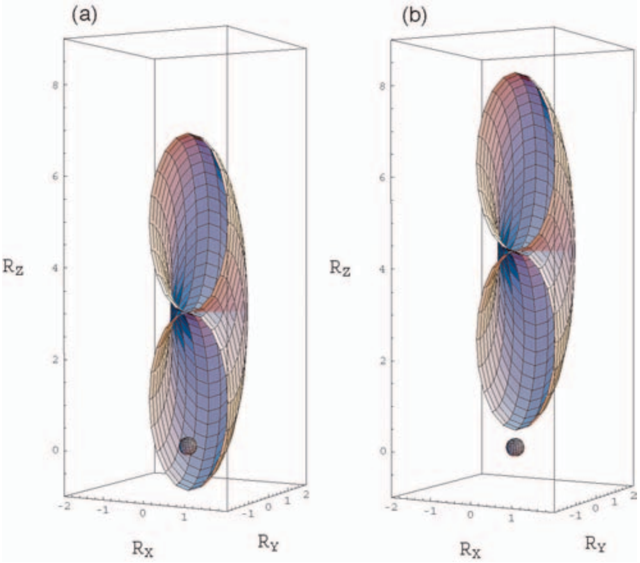

Fig. 1. Formally, we can treat a three-dimensional superconductivity as a collection of two-dimensional systems parametrized by, say, k_z. The superconducting node can be considered as the critical point of the quantum phase transition of the two dimensional systems between two states with different topological orders.Here we illustrate a example of the two-dimensional systems at (a)$k_z = 0$ and (b)$k_z = -2\pi/5$. A point node exists between these k_z's.

bers are analyzed. As for the unitary superconductors, condensed matter realizations of chiral anomalies for non-Abelian connections are given explicitly.Topological consideration is useful to distinguish superconductivities with the same pairing symmetry. Our analysis also clarified nodal structures of superconducting gaps with various anisotropic order parameters, which is closely related to the quantum Hall effect in three-dimensions. Various types of the nodal structures are not accidental but have fundamental topological origins.

References
[1] Y.Aharanov and D.Bohm, Phys. Rev. **115**, 485 (1959).
[2] T.Eguchi, P.B.Gilkey, and A.J.Hanson, Phys.Rep. **66**, 213 (1980).
[3] M.V.Berry, Proc.R.Soc. A 392, 45 (1984).
[4] D.J.Thouless, M.Kohmoto, P.Nightingale, and M.den Nijs, Phys. Rev. Lett. **49**, 405 (1982).
[5] M.Kohmoto, Ann. Phys. (N.Y.) **160**, 355 (1985).
[6] R.B.Laughlin, Phys. Rev. Lett. **50**, 1395 (1983).
[7] X.G.Wen, Phys. Rev. B**40**, 7387 (1989).
[8] T.Sentil, J.B.Marston, and M.Fisher, Phys. Rev. B**60**, 4245 (1999).
[9] Y.Hatsugai, S.Ryu, and M.Kohmoto, cond-mat/0308332.

Movie of the Nuclear Wave-packets

T. Suemoto

Since the pioneering work for NaI by Zewail's group [1], observations of the wave-packet (WP) oscillations have been reported for a number of molecules. One of the interesting challenges is to capture directly the time-evolving shape of the WP propagating on the potential surface. However, in most of the experiments up to now, the oscillatory behavior has been observed only at one or few points on the adiabatic potential surface. Therefore, the shape of the wave-packet had to be estimated from the temporal behavior of the signal observed at certain point with an aid of theoretical model.

Here, we present a demonstration of making a movie of the WP, showing the time development of entire WP shape moving on the potential surface [2]. In contrast to previous experiments, our method is direct and completely model-free.

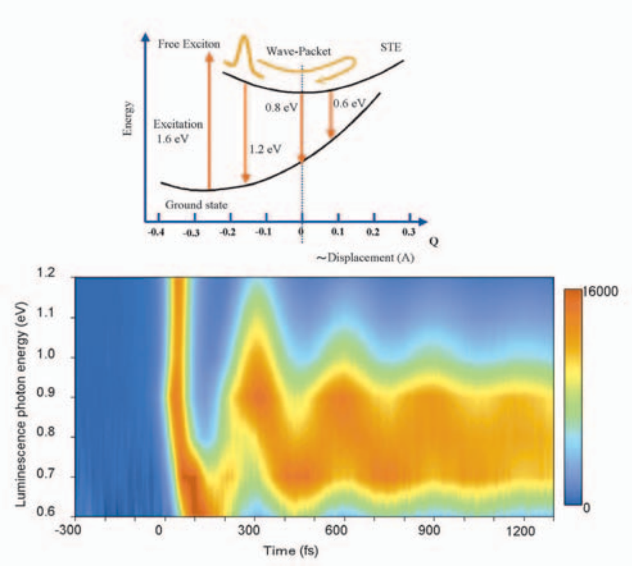

Fig. 1. The upper panel shows the adiabatic potential curves of STE in the Pt-Br complex. The abscissa corresponds to the displacement of the Br$^-$ ion. The lower panel is a two dimensional display of the time evolution of the luminescence intensity which can be regarded as the amplitude of the wave-packet. The ordinate is the luminescence photon energy, which approximately corresponds to the spatial position of the Br$^-$ ion.

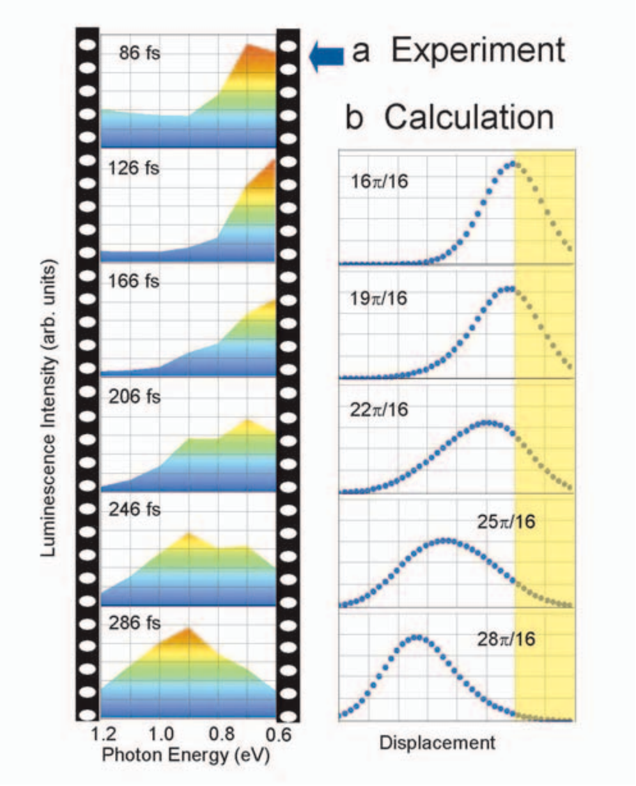

Fig. 2. A movie of the wave packet. The pictures in the column **a** are the vertical cross-sections cut from the 2D-plot shown in Fig. 1. The frames are taken every 40 fs. The curves in the column **b** are the calculation based on a harmonic oscillator model. The scales are adjusted to match the experimental data in the column **a**. The area not observed in our experiment is covered by yellow color.

We used single crystals of the halogen-bridged mixed-valence platinum complex $[Pt(en)_2]$ $[Pt(en)_2Br_2]$ $(ClO_4)_4$ (en=ethylenediamine), which is known as a prototype of the quasi-one-dimensional system. The adiabatic potential curves for the ground state and the self-trapped-exciton (STE) on a configuration coordinate are shown in Fig. 1. By observing the hot luminescence, we can obtain the shape of the wave-packet directly. The time evolution of the luminescence was investigated at ambient temperature using a frequency up-conversion technique with a time resolution of 50 fs. After a careful correction against the spectral response of the measurement system, we plotted the 7 × 240 data on a plane of the photon energy and the time delay in a color scale as shown in the lower part of Fig. 1. We can clearly see the sinusoidal motion of the WP around 0.8 eV.

From vertical cross-sections of this plot, we can obtain a movie, which is the first demonstration of real time capturing of the wave form within our knowledge. Here we can show some impressive snapshots taken every 40 fs on the left column in Fig. 2. We can see not only the oscillation, but also the change of the shape. That is, the peaks are flat at the center of oscillation (246 fs) and become sharp and asymmetric at the turning points (126, 286 fs). These features are well reproduced in the calculation based on a harmonic oscillator as shown on the right column in Fig. 2.

This reliable method of capturing the wave-packet form will be useful for investigating the dynamical behavior of the atomic motions including the de-coherence process and also for developing coherent control method of chemical reactions in molecules and lattice rearrangements in solids.

References
[1] A. H. Zewail, J. Phys. Chem. A **104**, 5660 (2000).
[2] T. Matsuoka,J. Takeda, S. Kurita and T. Suemoto, Phys. Rev. Lett. **91**, 247402 (2003)

Authors
Taira Matsuoka, Tohru Suemoto, Jun Takeda[a], and Susumu Kurita[a]
[a] Yokohama National University

Structural Study of the Si(111)$\sqrt{3}\times\sqrt{3}$-Ag Surface at Low Temperature by X-ray Diffraction

T. Takahashi

The Si(111)$\sqrt{3}\times\sqrt{3}$-Ag surface has been attracting interest since the frist observation of the surface by low energy electron diffraction in 1960s. Its structure had been controversial until a honeycomb-chained triangle (HCT) model as shown in Fig. 1(a) was proposed by surface X-ray diffraction [1]. Recently, however, it is suggested that the most stable structure of the Si(111)$\sqrt{3}\times\sqrt{3}$-Ag surface is not the HCT structure but an inequivalent triangle (IET) structure shown in Fig. 1(b) by the study of first-principles calculations and scanning tunneling microscopy (STM) at low temperatures [2].

The IET model is characterized as a structure in which large triangles of Ag atoms indicated by red broken lines in the HCT model rotate slightly around their centers, losing the mirror symmetry. The proposal of the IET model also casts some question about the structure at room temperature (RT), and suggests a possibility of a model in which Ag atoms thermally fluctuate at RT between two IET structures rotated in opposite directions, illustrated in the right down part of Fig. 1(b).

In this work [3], we investigate the in-plane structure of the surface both at RT and at low temperature using surface x-ray diffraction in the grazing incidence geometry. We have observed the intensities of diffraction spots peculiar to the $\sqrt{3}\times\sqrt{3}$ structure both at RT and at a low temperature of 50K. Experiments were done at PF-BL15B2. Figures 2(a) and 2(b) show the Patterson maps calculated from the observed intensities at RT and 50K, respectively. Since peaks in the Patterson map correspond to the interatomic vectors between two atoms, peaks A observed at RT are assigned to the interatomic vector between Ag atoms making large triangles in Fig. 1(a) as marked by A. In contrast, the peaks A split into two peaks A1 and A2 at 50K as shown in Fig. 2(b). This split indicates the existence of twin domains in which triangles of Ag atoms are rotated in opposite directions. This result is also supported from the observation of diffuse scattering originating from twin domains at low temperatures.

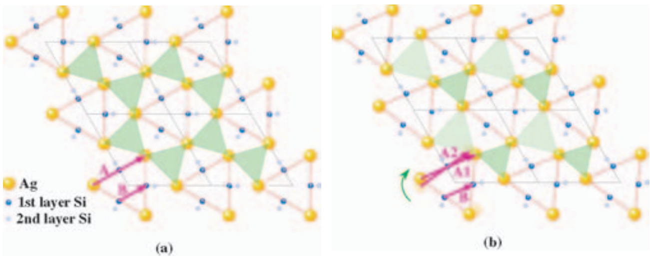

Fig. 1. Illustration of the HCT model (a) and IET model (b). Gray lines show the unit cell. In the IET model, large triangles indicated by red broken lines rotate slightly from the symmetric positions in the HCT model. This rotation changes the size of small triangles indicated by light green. In the IET model, there exists the domain structure in which the large triangles are rotated in the opposite direction as illustrated in the right down part.

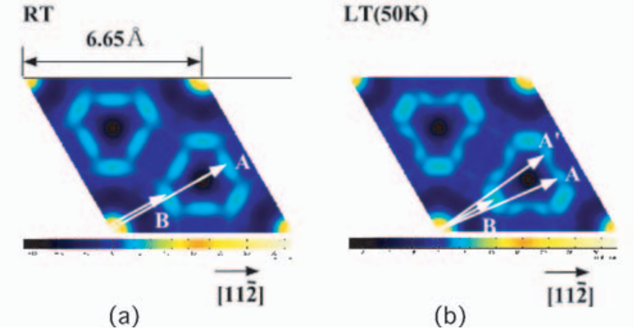

(a) (b)

Fig. 2. Patterson maps calculated from observed intensities at RT(a) and at 50K(b). Peaks A at RT, corresponding to interatomic vectors between Ag atoms, split into two peaks A1 and A2 at 50K. Peaks B correspond to interactomic vectors between the first-layer of Si atoms.

We have also determined the phase transition temperature to be about 150K from the temperature dependence of the diffuse scattering. Temperature dependence of some diffraction spots indicates that the phase transition is accompanied by structural changes. That means the structure at RT is not explained by the model in which Ag atoms thermally fluctuate between the two IET structures rotated in opposite directions. The analysis of the data observed at RT also supports the HCT model.

References
[1] T.Takahashi et al., Jpn. J. Appl. Phys. Part 2 **27**(1988) L753.
[2] H. Aizawa et al., Surf. Sci. **429** (1999) L509.
[3] H. Tajiri et al., Phys. Rev. B**68** (2003) 035330.

Authors
T. Takahashi, H. Tajiri[a], K. Sumitani, and K. Akimoto[b]
[a] JASRI
[b] Nagoya University.

Intersubband Absorption Linewidth in GaAs Quantum Wells

H. Akiyama

Effects of scattering mechanisms on intersubband absorption linewidth in GaAs QWs are studied quantitatively. Figure 1 shows an intersubband absorption spectrum of a modulation-doped 8-nm GaAs/AlAs single QW with a sheet electron concentration N_S of 9.8×10^{11} cm^{-2} (see the inset), measured at 4.5 K using a Fourier transform infrared spectrometer with a microscope (μ-FTIR). The linewidth $2\Gamma_{\rm op}$ was 11.1 meV and this is about an order of magnitude larger than the transport energy broadening $2\Gamma_{\rm tr}$ of 1.2 meV, to which mobility μ of 2.9×10^4 cm^2/Vs corresponds through transport relaxation time. Temperature dependences of the linewidth $2\Gamma_{\rm op}$ and transport broadening $2\Gamma_{\rm tr}$ are plotted in Fig. 2 by red and blue circles, respectively. Little correlation [1] was found between them in the temperature range from 4.5 to 300 K.

We calculated absorption linewidth using Ando's microscopic theory [2], which is similar to the conventional method of calculating transport mobility. In Fig. 2, calculated values of the linewidth $2\Gamma_{\rm op}$ and transport broadening $2\Gamma_{\rm tr}$ are shown by the various curves, where relevant con-

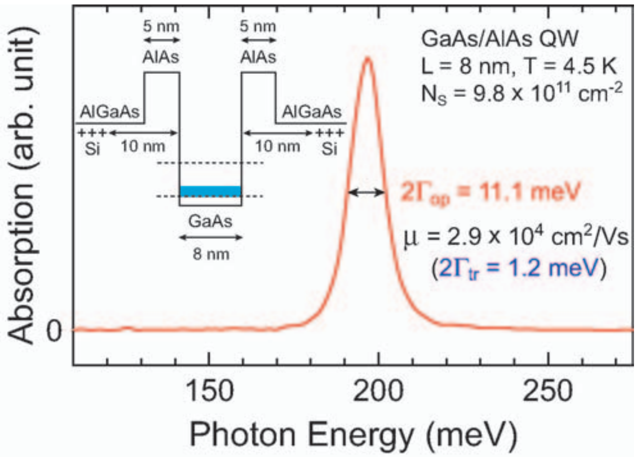

Fig. 1. The intersubband absorption spectrum of a modulation-doped 8-nm GaAs/AlAs single QW measured at 4.5 K using a μ-FTIR. Note that its linewidth $2\Gamma_{op}$ = 11.1 meV is an order of magnitude larger than the transport energy broadening $2\Gamma_{tr}$ = 1.2 meV, to which the mobility μ = 2.9 × 10^4 cm^2/Vs corresponds. The inset shows the structure of the QW.

tributions of interface roughness (IFR; with a mean height Δ of 0.4 nm and a correlation length Λ of 4.3 nm), LO phonon, and LA phonon scattering are included one by one (see legend). Satisfactory agreement between the experimental data and the theoretical calculations was obtained for both absorption linewidth and mobility.

Therefore, the apparent lack of correlation [1] between absorption linewidth and mobility is confirmed and consistently explained. At low temperatures, interface roughness scattering dominates both $2\Gamma_{op}$ and $2\Gamma_{tr}$, and the $2\Gamma_{op}$ of 10.4 meV is about an order of magnitude larger than the $2\Gamma_{op}$ of 1.2 meV. This is because the contribution from intrasubband scattering in the first excited subband is much larger than that in the ground subband [3]. As a result of the significantly different effects of interface roughness and LO phonon scattering [3], absorption linewidth has little correlation with mobility.

Very recently, we have succeeded in measuring intersubband electronic Raman scattering in narrow GaAs-based single QWs such that the intersubband energy separation is more than ~ 150 meV [4]. We are discussing a relation between intersubband absorption and Raman scattering in terms of transition energy and linewidth.

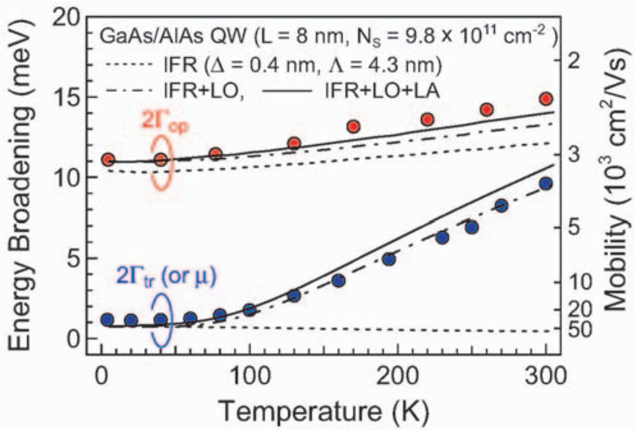

Fig. 2. Temperature dependences of the absorption linewidth $2\Gamma_{op}$ and transport broadening $2\Gamma_{op}$ (or mobility μ). Measured values are plotted by circles, and calculated ones are shown by lines, in which the contributions of interface roughness (IFR), LO phonon, and LA phonon scattering are considered.

References

[1] K. L. Campman, H. Schmidt, A. Imamoglu, and A. C. Gossard, Appl. Phys. Lett. **69**, 2554 (1996).
[2] T. Ando, J. Phys. Soc. Jpn. **44**, 765 (1978); **54**, 2671 (1985).
[3] T. Unuma, M. Yoshita, T. Noda, H. Sakaki, and H. Akiyama, J. Appl. Phys. **93**, 1586 (2003); T. Unuma, T. Takahashi, T. Noda, M. Yoshita, H. Sakaki, M. Baba, and H. Akiyama, Appl. Phys. Lett. **78**, 3448 (2001).
[4] T. Unuma et al., unpublished.

Authors

Takeya Unuma, Masahiro Yoshita, Takeshi Noda[a], Hiroyuki Sakaki[a], and Hidefumi Akiyama
[a] Institute of Industrial Science, University of Tokyo

Lasing in a Single Quantum Wire

H. Akiyama

We fabricated a single quantum wire with a small cross-sectional size of 14 nm by 6 nm and significantly reduced size variation over the whole cavity length of 0.5 mm [1], and achieved lasing in the wire ground state. This is the thinnest laser in the world.

The single quantum wire laser is fabricated by an advanced crystal growth method called the cleaved-edge overgrowth method (CEO) with molecular beam epitaxy (MBE), in which two MBE growth steps are separated by an *in situ* wafer cleavage process. Figure 1 shows a schematic cross-sectional view of the single wire laser structure. In the first MBE growth, we grew a 14 nm quantum well (stem well) at 600 °C on a non-doped (001) GaAs substrate. Then, we cleaved the wafer, and grew a 6 nm GaAs quantum well (arm well) at 490 °C on an in situ cleaved fresh (110) edge of this structure. After the growth of the arm well, we interrupted growth and annealed the GaAs surface for 10 minutes at 600 °C. At a T-shaped intersection of a stem well and an arm well, quantum-mechanical confinement of electrons forms a quantum wire. The blue contour curves show the probability of 1-D electrons in a quantum wire. This quantum wire has no higher 1-D subband, and is in the 1-D quan-

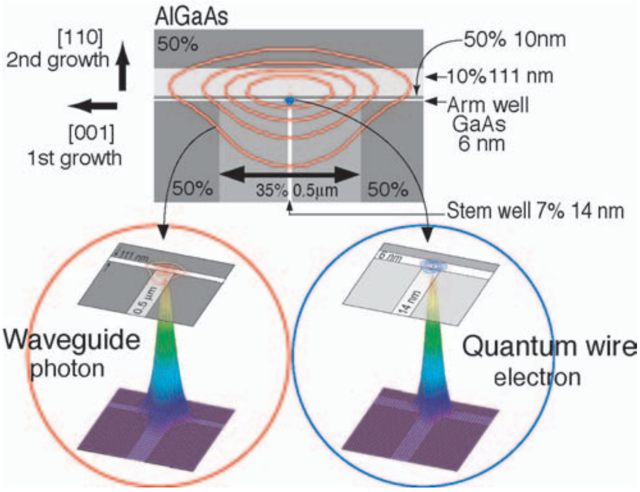

Fig. 1. Schematic cross-sectional view of a single wire laser structure. Percentages show Al-concentration x in $Al_xGa_{1-x}As$. A quantum wire is formed at a T-intersection of a 14 nm thick $Al_{0.07}Ga_{0.93}As$ stem well and a 6 nm thick GaAs arm well, which is embedded in a core of T-shaped optical waveguide formed by a 500 nm $Al_{0.35}Ga_{0.65}As$ stem layer and a 111 nm $Al_{0.1}Ga_{0.9}As$ arm layer. The squared wave functions, or probability, of photons and electrons in the device are drawn by contour curves, which show that photons and electrons are confined at the T-intersections. The thick arrows indicate [001] and [110] axes for the first and second MBE growth.

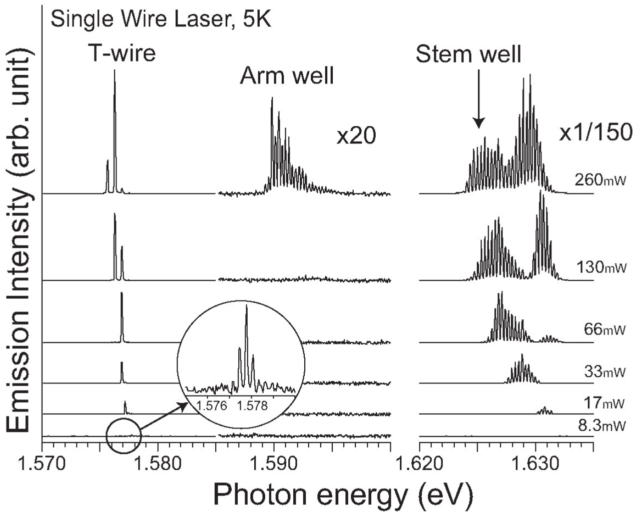

Fig. 2. Lasing spectra of the single quantum wire laser at 5K for the various input powers of P_{in}=8.3, 17, 33, 66, 130 and 260 mW, measured with spectral resolution of 0.2 meV. Lasing lines due to the quantum wire, the arm well, and the stem well are observed. The lasing of the quantum wire has excellent characteristics of a low threshold, a single lasing mode, and small red shifts.

tum limit.

The sample was pumped optically with an excitation light focused via the top surface of the structure shown in Fig. 1. Figure 2 shows laser emission spectra from the device at 5K for various excitation input powers P_{in}. At input power P_{in}=8.3 mW, multi-mode laser emission of the quantum wire is observed at 1.578 eV. It changes to single-mode at P_{in}=17 mW, and shows slight red shifts with mode hopping as the input power increases. The amount of red shifts is 1.5 meV at P_{in}=260 mW. At higher energies, laser emissions from the arm well and the stem well are also observed. We observed lasing of this quantum wire laser at 5 – 60 K. Our 1-D quantum wire provided an opportunity to study many interesting fundamental issues in 1-D systems.

Reference

[1] Y. Hayamizu, et al. Appl. Phys. Lett. **81**, 4937, (2002); Y. Hayamizu, et al. Proc. 26th Int. Conf. on Phys. of Semiconductors (2003).

Authors

Y. Hayamizu, M. Yoshita, S. Watanabe, H. Akiyama, L. N. Pfeiffer [a], and K. W. West [a].
[a] Bell Laboratories, Lucent Technologies

Intrabeam-scattering and Radiation-damping Effects Observed with a Developed Beam Profile Monitor

N. Nakamura

We have developed a high-resolution beam profile monitor based on an X-ray imaging optics with two FZPs in the KEK-ATF damping ring in order to measure an electron beam size less than 10 μm [1,2]. The synchrotron radiation (SR) from the electron beam at the bending magnet is monochromatized by a Si(220) crystal monochromator and the electron beam profile is twenty-times magnified by two FZPs and detected on an X-ray CCD camera. The spatial resolution is about 0.6 μm (1σ) for the selected photon energy of 3.235 keV. After successfully obtaining an electron beam image, we started to observe various beam behaviors in the ring with this monitor system.

Figure 1 shows time dependence of the measured vertical beam size after injection from the injector linac to the ring, in addition to three transverse beam images. The X-ray

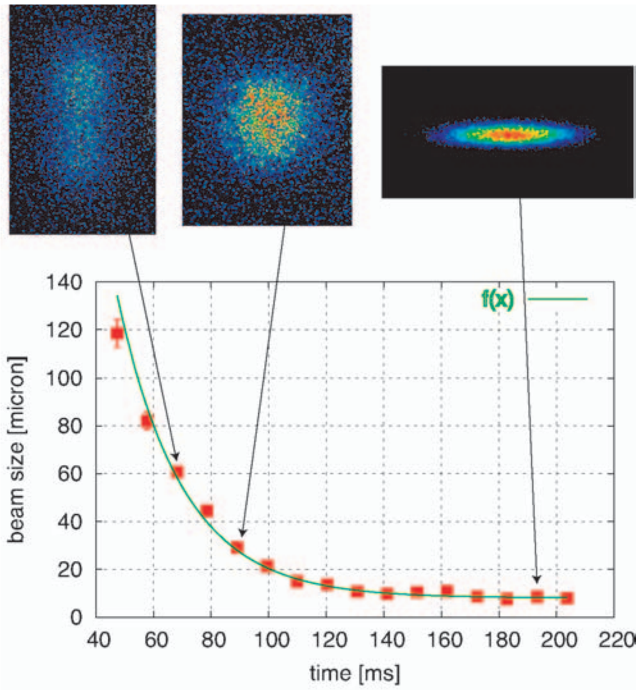

Fig. 1. Time dependence of the measured vertical beam size after injection from the injector linac to the ring. The beam started to shrink after the injection and finally reached the equilibrium state in the ring. This resulted from the radiation damping.

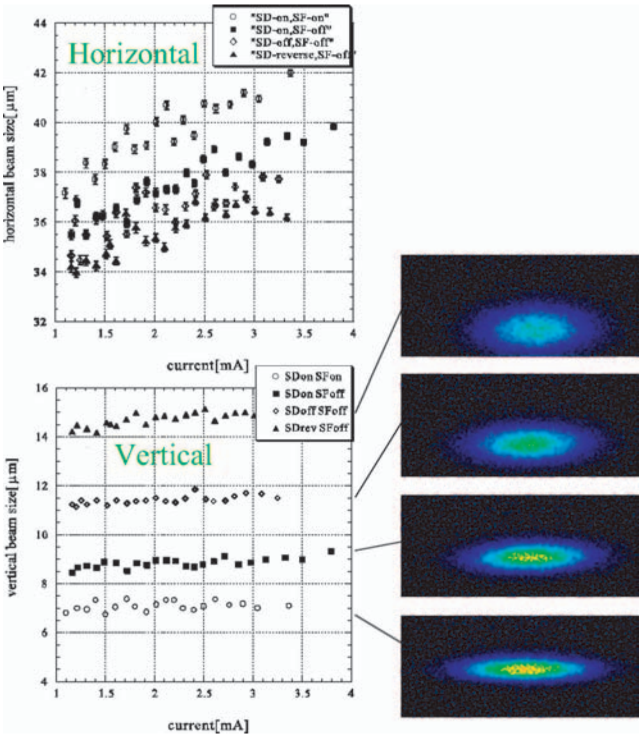

Fig. 2. Current and coupling dependencies of beam size measured by the beam profile monitor. The horizontal beam size increased with bunch current because of the intrabeam scattering. Four beam images show that the horizontal and vertical beam sizes correlatively change with the emittance coupling.

CCD camera and the X-ray shutter were synchronized with the injection trigger signals. The vertical beam size decreased with time after injection and then reached the equilibrium state, as shown in Fig. 1. The beam shrink is due to the radiation damping effect. The radiation damping time was obtained by fitting the time dependence to an exponential curve to be about 25 ms. This is in good agreement with the design value.

Low-emittance and low-energy rings such as the ATF damping ring and the Super-SOR light source can be affected by intrabeam scattering, which causes increase of beam size with bunch current. Figure 2 shows bunch current dependences of the horizontal and vertical beam sizes measured by the beam profile monitor. The horizontal beam size significantly increased with bunch current because the momentum spread increased due to intrabeam scattering and the SR source point had a considerable horizontal momentum dispersion. The coupling dependences were also measured by changing currents of the skew-quadrupole coils wound on two kinds of sextupole magnets, "SD" and "SF". As shown in Fig. 2, the vertical beam size increased with the emittance coupling, while the horizontal one decreased. The emittance coupling effect was clearly found in this experiment.

References
[1] K. Iida et al., Nucl. Instr. and Meth. A 506 (2003) 41-49.
[2] N. Nakamura et al., Proc. of 8th International Conference on Synchrotron Radiation Instrumentation: AIP Conference Proceedings 705, San Francisco, pp.545-548, 2003.

Authors
N. Nakamura, H. Sakai, H. Takaki, T. Muto[a], and H. Hayano[a]
[a] *High Energy Accelerator Research Organization (KEK)*

Development of Scanning Tunneling Microscope Combined with Synchrotron Radiation Light Source for Elemental Analysis

T. Kinoshita and Y. Hasegawa

Scanning tunneling microcopy (STM) provides us information on atomic structure of material surfaces with high spatial resolutions. It is, however, not easy to obtain chemical or elemental information except a few special cases such as inelastic tunneling spectroscopy. The reason is simply because STM probes tunneling current which basically reflects valence electronic states of a sample. In order to access elemental information, one needs to probe core-level electrons as Auger and x-ray photoelectron spectroscopy do. In this project, we constructed an ultrahigh vacuum (UHV) STM with which one can excite core-level electrons with synchrotron radiation (SR) light source and pick them up by the probe tip (SR-STM) (Fig. 1) [1]. Advantages of using SR light source are, in addition to its high intensity, that the energy of the light can be tuned so that one can excite core electrons of a specific element, advantageous for the elemental identification.

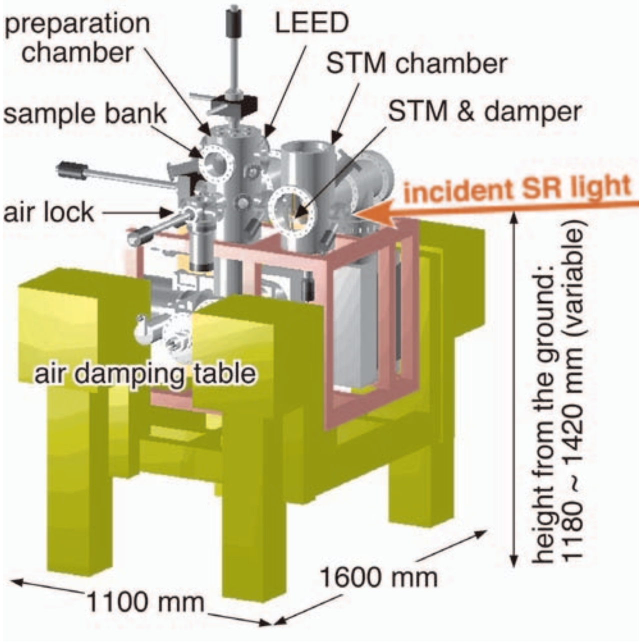

Fig. 1: schematic of SR-STM

We first tested a performance of the system by using a standard sample of the Si(111)- 7×7 surface. All experiments were carried out at BL-19A, Photon Factory, KEK, Japan. In spite of the mechanically and electronically noisy conditions, we successfully took atomically resolved images of the surface, implying a stability of our system as a UHV-STM. We then checked a detection of photo-emitted electrons excited from core states with the tip. To test this, we took STM images of the Si surface under the SR illumination with its photon energy varied from 96 eV to 106 eV. The Si 2*p* adsorption edge (99 eV) is in the photon energy range. When the photo-emitted electrons are detected by the tip, the tip is retreated from the surface, trying to keep the total current constant, and consequently the image looks high (bright) (Fig. 2). We found a sharp increase in height at the edge energy, indicating the detection of the excited core electrons. This result demonstrates the possibility of elemental identification using this technique.

References
[1] T. Matsushima, T. Okuda, T. Eguchi, M. Ono, A. Harasawa, T. Wakita, A. Kataoka, M. Hamada, A. Kamoshida, Y. Hasegawa and T. Kinoshita, Rev. Sci. Instrum. **75** 2149 (2004).

Authors
T. Matsushima, T. Okuda, T. Eguchi, M. Ono, A. Harasawa, T. Wakita, A. Kataoka, M. Hamada, A. Kamoshida, Y. Hasegawa, and T. Kinoshita

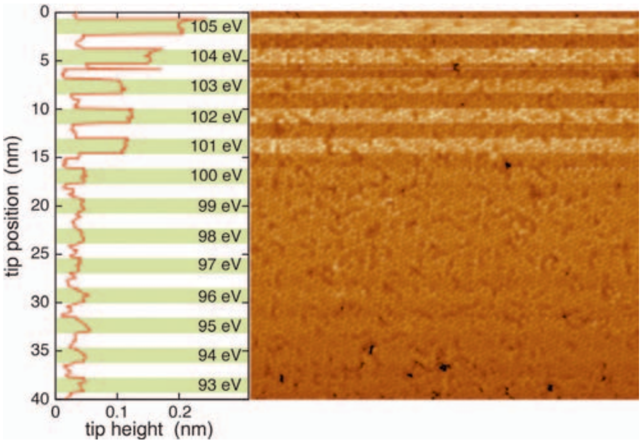

Fig. 2 STM image (right) of the Si(111)7×7 surface. During taking this image, the sample was irradiated with a light coming from synchrotron radiation light source. The light energy was changed from 93 eV at the bottom of the image to 105 eV on the top. The averaged height of the image was plotted in the left-side panel.

Surface Magnetism of Graphite in Liquid ^{3}He

H. Ishimoto

The adsorbed ^{3}He (S=1/2) on the well defined surface is a fruitful system to study two-dimensional magnetism. In particular ^{3}He film adsorbed on graphite has extensively been studied owing to the atomically flat surface and large surface area of graphite. According to recent studies on the film, the layer by layer growth is confirmed up to 7 layers at least and the first and the second atomic layer solidify on the graphite surface, while the upper layers above the second one exist as a liquid. The motion of ^{3}He atoms in the solid layer is considered to be restricted to a two dimensional plane, since the binding energy is evaluated to be about 135 K and 65 K for the first and the second layer, respectively, much larger compared with the temperature for measurements. Therefore, a magnetism for the first or the second layer is understood as a consequence of an ideal two-dimensional magnet with multiple spin exchange (MSE) interactions. The exchange of even number of particles is anti-ferromagnetic (AFM), while that of an odd number is ferromagnetic (FM). The competition between them causes evolution from anti-ferromagnetism to ferromagnetism as a function of the areal density. In addition to the intra layer interactions, there is a long standing controversy on a possible indirect interaction mediated by ^{3}He quasi-particle in the over-layer liquid. Theoretically various models are proposed based on a second order perturbation theory, for example, the quasi-localized-Fermion theory etc.. Most of the models predict the existence of RKKY (Ruderman-Kittel-Kasuya-Yoshida) type indirect exchange interaction. Experimentally, the recent experiments on the adsorbed film suggest a rather small contribution of this type of interaction.

However on the boundary surface dipped in the bulk liquid ^{3}He, there is no clear evidence so far. Here we present the first systematic study with a cw NMR technique for the solid ^{3}He layer on graphite covered with bulk liquid ^{3}He as a function of liquid pressure between 0.6 and 31.38 bar.

After subtracting the liquid contribution, the nuclear magnetization corresponding to the solid layers on the Grafoil surface shows a strong ferromagnetic tendency with a periodic behavior as function of liquid pressure. The first layer is known to be paramagnetic and the ferromagnetic tendency in the second layer is too small to reproduce the observed behavior. The other possibility is the solidification of third and fourth layer with increasing the liquid pressure, analogous to the liquid pressure dependent epitaxial adsorption of solid ^{4}He up to seven layers. The detailed analysis gives the pressure dependence of the Weiss temperature as shown in Fig.1, indicating that the third layer is completed at 19 bar and the fourth at 25 bar. The number of localized spins estimated from the solid magnetization is almost doubled from 0 bar to 25 bar, being consistent with this scenario.

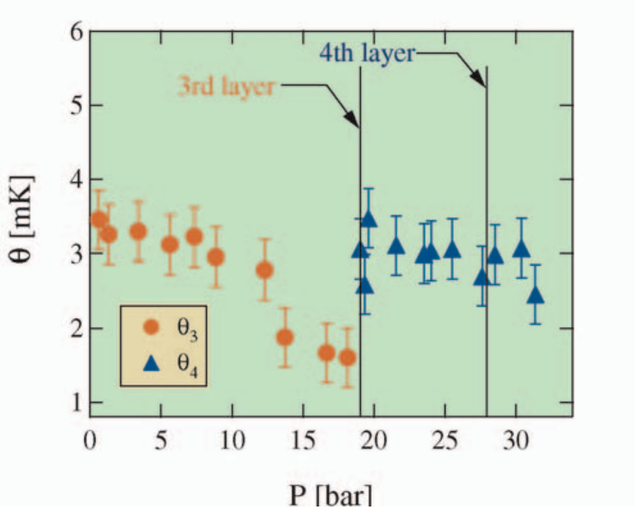

Fig. 1. Pressure dependence of the Weiss temperature for third and fourth layer.

Rotation-induced 3D Vorticity in Superfluid Monolayer ^{4}He Films Condensed in a Porous Glass

M. Kubota

Superfluid ^{4}He films adsorbed in porous media provide a unique possibility to study the interplay between 2D and 3D physics [1]. Especially for the superfluid transition, the system shows similar behavior to the 2D film (the Kosterlitz-Thouless transition [2]) such as the density proportional super-fluid transition temperature T_c, with the energy dissipation peak around T_c [3]. Whereas the superfluid density's critical index is found close to 2/3 of 3D systems[1,4] and a sharp cusp of the specific heat[5] appearing around T_c, which is similar to the transition of the bulk ^{4}He λtransition.

A crucial role in the Kosterlitz -Thouless 2D transition[2] belongs to thermally excited vortex-antivortex pairs (VAPs). However multiple connectivity of the superfluid film in porous media allows a variety of vortex configurations other than VAP, e.g., vortex rings and 3D coreless pore vortices [7 - 9]. For bulk liquid ^{4}He 3D superfluid transition, a mechanism is proposed where the vortex rings play the important role [6]. Therefore one may expect that the

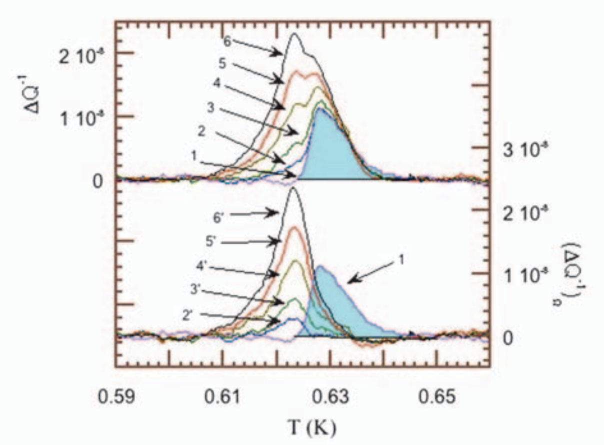

Fig. 1. Energy dissipation peak under rotation (a), the number from 1 to 6 each corresponds to rotation speed 0, 0.79,1.57, 3.14, 4.71, 6.28 rad/sec respectively. It is realized that the data in (a) is actually the summation of the two peaks,namely the static peak and and a rotationally induced peak,by subtracting the static peak 1 from the data displayed in (a). Rotationally induced peak ($\Delta Q^{-1}{}_{\Omega}$) is displayed in (b) together with the static peak with dashed number, each corresponding to the number in (a). Data are all for the film with the superfluid transition temperature T_c=628mK, which is determined as in [3]. See also Fig. 2 caption.

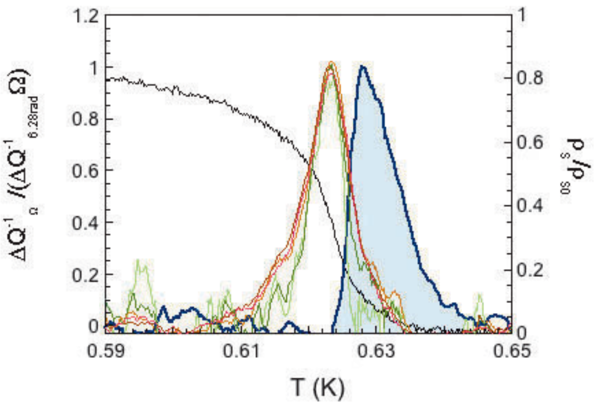

Fig. 2. The right side (high T) peak is the one appears in static condition. The group of the left peaks is rotation-induced ones for various scaled (divided) by *Ω*. The fact that all the curves collapse more or less on the same curve proves linearity on *Ω*. In addition, superfluid density scaled by its zero temperature value is displayed. The lagest slope is extrapolated to zero density to T_c=628mK where the static peak is also located[3].

response of the film on a porous substrate would be essentially different from that on a plane substrate, and observation under rotation should be quite interesting for understanding the role of these vortices on the superfluid transition.

With use of the world record rotational cryostat [10], the first clear evidence of rotationally induced vortex lines in such thin film superfluid formed in a porous glass substrate has been obtained. In ref.[11], a detailed study of torsional oscillator experiments under steady rotation up to 6.28 rad/sec is reported for a ^{4}He superfluid monolayer film formed in 1 μm-pore diameter porous glass. We found a new additional dissipation peak with the height being in proportion to the rotation speed, which is located to the lower temperature than the vortex pair unbinding peak observed in the static state. We propose that 3D coreless vortices (“pore vortices”) appear under rotation to explain this new peak. That is, the new peak originates from dissipation close to the pore vortex lines, where large superfluid velocity shifts the vortex pair unbinding dissipation to lower temperature. This explanation is confirmed by observation of nonlinear effects at high oscillation amplitude.

References

[1] J. D. Reppy, J. Low Temp. Phys. **87** 205 (1992) and references therein.
[2] J. M. Kosterlitz and D. J. Thouless, J. Phys. C**6**, 1181 (1973); Prog. Low Temp. Phys. B **7**, 373 (1978).
[3] K. Shirahama et al., Phys. Rev. Lett. **64**, 1541 (1990); Physica B **165-166**, 545 (1990).
[4] N. P. Mikhin et al., Physica B **329-333**, 272 (2003).
[5] S. Q. Murphy, J. D. Reppy, Physica B **165** Part 1, 547 (1990).
[6] G. A. Williams, Phys. Rev. Lett. **82**, 1201 (1999); ibid **68**, 2054 (1992).
[7] T. Minoguchi, Y. Nagaoka, Prog. Theor. Phys. **80**, 397 (1988).
[8] J. Machta and R. A. Guyer, Phys. Rev. Lett. **60**, 2054 (1988); J. Low Temp. Phys. **74**, 231 (1989).
[9] T. Obata, M. Kubota, Phys. Rev. B **66**,140506 (2002).
[10] V. Kovacik et al., J. Low Temp. Phys. **101**, 567 (1995).
[11] M.Fukuda, M. Zalalutdinov, V. Kovacik, T. Minoguchi, T. Obata, M. Kubota, and E. Sonin, :cond-mat/0405092/May 2004.

Authors
M. Fukuda[a], M. Zalalutdinov[b], V. Kovacik[c], T. Minoguchi[d], T. Obata, M. Kubota, and E. Sonin[e]
[a] Central Research Lab.Hitachi Ltd
[b] Physics Dept. Cornell Univ.
[c] KOHZU Precision Co, Ltd.
[d] Inst. Physics, Univ. Tokyo
[e] Racah Institute, Hebrew Univ. of Jerusalem.

Magnetotransport Studies under Pulsed Ultra-High Magnetic Fields Using RF Techniques

T. Osada

(1) Fractional Quantum Hall Effect Observed in Ultra-High Magnetic Field Range

Two dimensional (2D) electron systems has been expected to show various electronic states under ultra-high magnetic fields where the filling factor *ν* is much smaller than 1; fractional quantum Hall state, composite Fermion state, even denominator state (pairing state), Wigner crystal state, Hall insulator state, *etc*. To clarify the high field phase diagram of the 2D electron system, we have tried the transport measurement of 2D systems under pulsed ultra-high magnetic fields employing the RF reflection coefficient method.

In this case, there is additional technical difficulty. The impedance of 2D systems becomes too large (>> 1M *Ω*) to measure using RF under ultra-high fields. Such high impedance is out of range of the sensitivity of RF reflection coefficient method, and it becomes easy to be affected by the stray capacitance of the system. To avoid the above problems, we have fabricated a Corbino-type device with modified electrode geometry as shown in the inset of Fig. 1. This device has large electrode perimeter and short electrode distance to decrase the device impedance wherever possible.

Figure 1 shows the diagonal conductivity σ_{xx} of GaAs/AlGaAs heterointerface with the mobility of ~2.4x10^5 cm^2/Vs measured under pulsed ultra-high field generated by the single-turn coil method. We can see two dip structures at field positions corresponding to *ν*=1 and *ν*=1/3. This is the highest field measurement which have observed the fractional quantum Hall effect. In spite of high temperature T > 4.2 K, the *ν*=1/3 structure could be observed since the energy gap is enhanced (Δ ~ 50 K) at ultra-high magnetic fields (B ~ 80 T). The present result is promising one for future studies on quantum Hall systems under ultra-high magnetic fields.

(2) Carbon Substitution Effect of a Novel Superconductor MgB_2

We have investigated the carbon substitution effect on a novel two-gap superconductor MgB_2. Since carbon substitution has strong influence on both of the electronic structure and impurity scattering rate, its superconducting properties are substantially modified. Microcantilever torque measurements revealed that the upper critical field H_{c2} is greatly

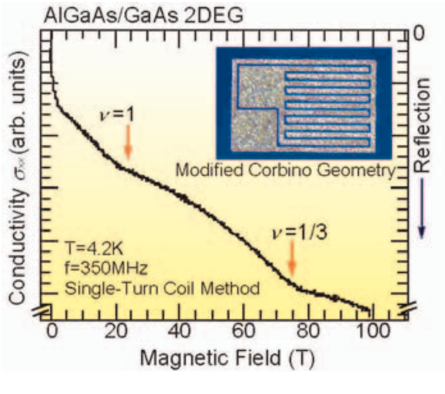

Fig. 1. Diagonal conductivity σ_{xx} of two-dimensional electron gas in the ultra-high magnetic field range. Inset: modified sample geometry.

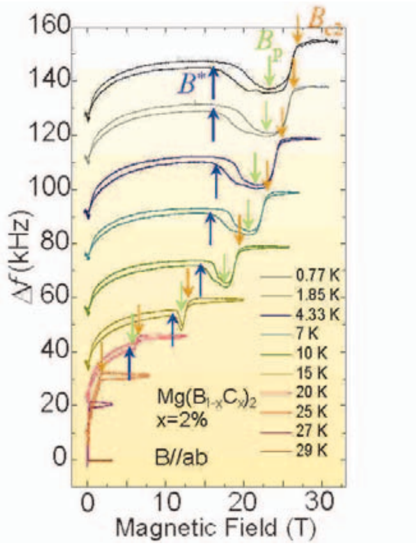

Fig. 2: Surface impedance of $Mg(B_{1-x}C_x)_2$ measured by the tunnel diode oscillator method.

enhanced by a factor of two ($\mu_0 H_{c2}$ (0) > 33 T) by 3-5% carbon substitution, though T_c monotonously decreases with carbon content. The enhancement is explained by a reduction in the inplane coherence length, while the T_c reduction is due to carrier doping. We also observed the temperature-dependent H_{c2}-anisotropy at all carbon contents. This fact strongly suggests that the two-gap superconductivity is less influenced by a small amount of carbon substitution, in contrast to theoretical predictions.

We have also studied the carbon substitution effect on the vortex phase diagram of MgB_2. Since carbon-substituted MgB_2 single crystals are very small (200-500μm), we have developed a high-sensitive RF technique with the use of a tunnel diode oscillator (Fig. 2), from which the effective penetration depth λ_{eff} is obtained. We demonstrate a systematic change of the peak effect with the carbon content. This result is accounted for by an impurity effect of carbon atom on the vortex order-disorder transition.

Authors
T. Osada, E. Ohmichi, S. Ikeda, T. Inokuchi, K. Kobayashi, T. Sekitani, M. Kobayakawa, A. Ogasawara, E. Komatsu, and K. Kajiki

Observation of Spin Gap and Superconducting Gap in a Spin Ladder Cuprates $Sr_2Ca_{12}Cu_{24}O_{41}$: NMR Study under High Pressure of 3.5GPa

Y. Uwatoko

$Sr_{14-x}Ca_xCu_{24}O_{41}$ (x=11.5-13.5) has been attracted a number of researchers because the system is the only spin-ladder compound which exhibits superconductivity. However, the superconductivity is realized only under high pressure above 3 GPa. This fact has been main hurdle to investigate the superconducting state, although investigation with using a variety of experimental methods is required not only for determination of the pairing symmetry but also for solution of spin-gap problem as is the case of high-Tc cuprates. High pressure above 3 GPa is usually attained by using a cubic-anvil or diamond-anvil pressure cell, and the measurements were limited on the macroscopic level such as resistivity or AC susceptibility measurement. A clamp-type pressure cell is much more convenient and available to various methods in which a larger sample volume is needed. However, usual clamp-type pressure cell is made of CuBe alloy and the maximum pressure is 3 GPa at most. Hence, the superconductivity has not been studied on the microscopic level for 7 years after the discovery of the superconductivity in 1996. We have improved clamp-type pressure cell using NiCrAl alloy, and succeeded in the microscopic study for the first time using ^{63}Cu nuclear magnetic resonance (NMR) [1]. This enabled us to study the pairing symmetry as well as the relation between the spin gap and the superconductivity.

The appearance of the superconductivity was confirmed by measuring resonance frequency of a NMR probe attached to the pressure cell. The resonance frequency is given as $f \propto 1/\sqrt{(LC)}$ where L and C represent inductance and variable capacitance of the NMR probe, respectively. The sample is contained in a coil and the onset of superconductivity is detected by the change of the resonant frequency, *i.e.* the change of L value. This method corresponds to an AC susceptibility measurement. T_c at 3.5 GPa is obtained to be 4.7 K which is consistent with that obtained from the resistivity measurement. The T dependence of f at several fields is shown in the inset of Fig. 1. If we probe the temperature at which the resonance frequency starts to change against $\boldsymbol{H}$, this gives Hc_2 vs. T_c characteristics as is shown in the main panel of Fig. 1. The conventional Pauli limit is calculated as 8.65 T by using the value of T_c at zero field. It should be remarked that the superconductivity is quite stable even under high field close to Pauli limit.

The NMR measurement at 3.5 GPa was performed by applying the magnetic field $\boldsymbol{H}$ parallel to the leg direction, crystal c axis to avoid influence of vortex motion. As shown

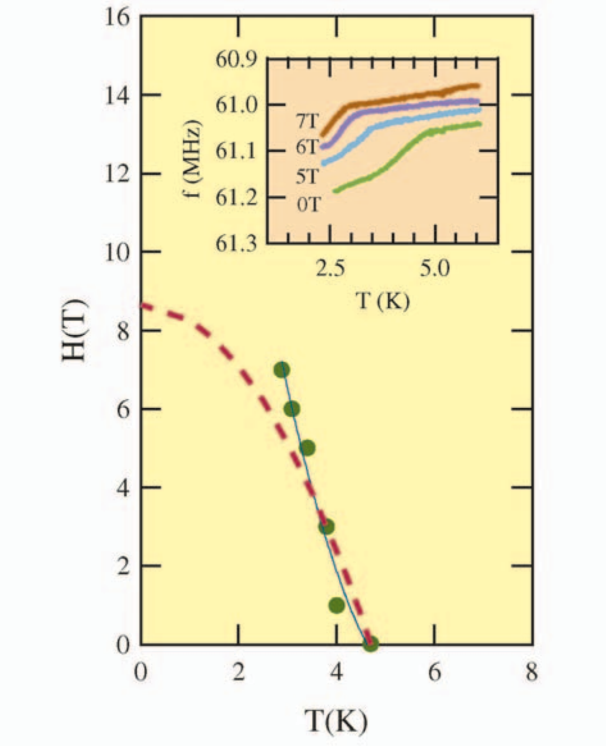

Fig. 1. H_{c2} –T_c characteristics obtained from resonance frequency (f) of a NMR probe. Conventional Hc-Tc curve is shown as a red broken curve. Pauli limit is calculated to be 8.65 T from the value of Tc at zero field. The inset shows raw data of the resonance frequency. The superconducting state is observed from the onset of f.

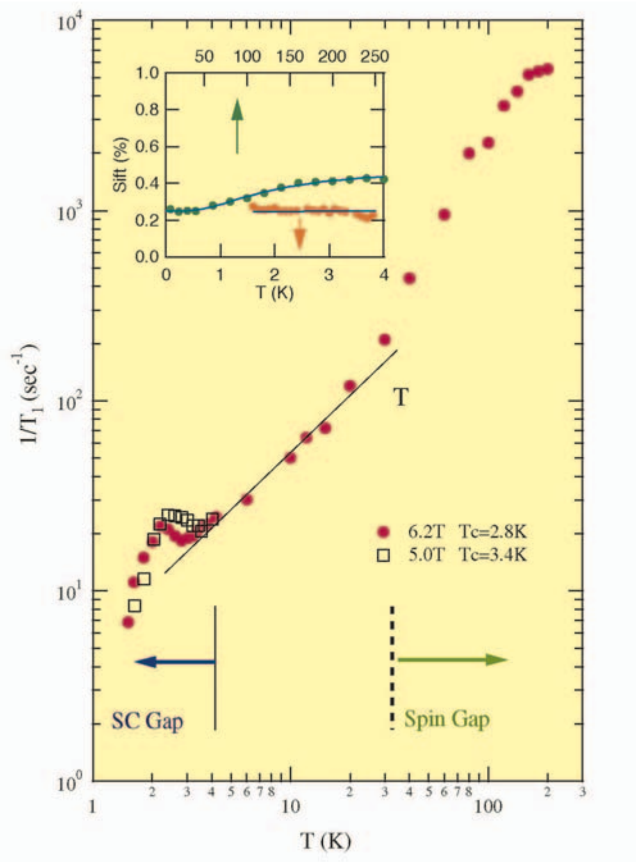

Fig. 2. The main panel shows relaxation rate (T_1^{-1}) of ^{63}Cu nuclei for the ladder site. Spin gap and superconducting gap are observed as an activated behavior and a hump at high T above 50 K and low T below 4K, respectively. The inset shows ^{63}Cu-NMR shift for the ladder site. Red points represent data taken precisely in a narrow T range between 1.4 K and 4 K, whereas Green points represent data taken in a wide T range. The blue curve which fit the green points represent theoretical curve for the insulating spin-ladder system.

in the main panel of Fig. 2, T_1^{-1} for the ladder site was measured at 70.0 MHz which corresponds to 6.2 T. (T_c at this field is about 2.8 K as is seen from Fig. 1.) The activated T dependence is observed at temperatures higher than 50 K, *i.e.*, $T_1^{-1} \propto exp\ (-\Delta_{spin} /T)$. The value of the gap Δ_{spin} is estimated to be 173 K. It should be noted that the spin-activation behavior is seen in the state in which the charge transport is metallic. By contrast, below 50 K T_1^{-1} is dominated by a Korringa-type T-linear term followed by a peak developed just below T_c. The appearance of the peak implies that a finite gap exists in the quasi-particle excitation at all wave vectors, namely no nodes across the Fermi surface. The peak is still observed even at high field close to the Pauli limit, which is not expected in conventional spin-singlet superconductors.

The inset of Fig. 2 shows T dependence of the NMR shift. The shift is given as a sum of two components, the orbital and the spin parts ($K=K_{orb} + K_{spin}$), and the spin part is proportional to the spin susceptibility. The T dependence of K at high temperatures fits well the theoretical curve for a spin ladder system, $K = K_0 + K_1 / \sqrt{T}\ exp(-\Delta_{spin}/T)$. The gap Δ_{spin} is obtained to be 217K and is comparable with that estimated from T_1^{-1}. The value of K_0 is estimated to be 0.25%. K_0 is expressed as $K_0 = K_{orb} + K_{para}$ where K_{orb} represents the orbital part and paramagnetic contribution corresponding to the Korringa term in T_1^{-1}, , respectively. Below T_c (=2.8 K at 6.2 T) the paramagnetic contribution should diminish toward T = 0, if spin-singlet superconductivity is realized. However, no appreciable change is seen around T_c as is shown in the precise data at low T. If the orbital part does not change drastically by applying pressure, K_{orb} is estimated to be 0.08% from the data at ambient pressure. Then, K_{para} is estimated to be 0.17%.

In the present work, we found that superconductivity with a full gap is realized and is quite stable even at high field close to Pauli limit. The fact excludes the possibility that conventional s-wave superconductivity is realized in this system. As for existence of a full gap, both d-wave and p-wave cases are possible if no nodes across the Fermi surface. However, in the case of d-wave superconductivity two questions should be resolved, namely one is why the NMR shift remains unchanged below Tc, and the other is why singlet pairing occurs again at low temperatures below Tc although spin-singlet pairing is already formed at high temperatures. As far as NMR results is concerned, p-wave with a full gap may be preferred.

The present work was partially supported by Grant-in-Aid for the Ministry of Education, Science and Culture, Japan, and by grants of Ogasawara Foundation for the Promotion of Science and Engineering, Japan and Simadzu Science Foundation, Japan.

Reference

[1] N. Fujiwara, et. al., Phys. Rev. Lett. **90** (2003) 137001.

Authors

N. Fujiwara, N. Môri, Y. Uwatoko, T. Matsumoto, N. Motoyama, and S. Uchida

---

Developments of Micro Pressure Cell and Specific Heat of Ce_2RhIn_8

I. Umehara and Y. Uwatoko

Strong correlated electron system under high pressure shows the variety of physical properties. Especially, specific heat measurement under pressure is the powerful tool to understand the ground state properties of strong correlated electron system under high pressure. We have developed the micro pressure cell for the measurements of specific heat, which can be also measured the magnetization in the commercial SQUID magnetometer. In this paper we report about design of our micro pressure cell and present the data of specific heat of Ce_2RhIn_8 under pressure.

Figure 1 shows the schematic drawing of micro cell, which we designed. An important change from previous one [1] is using a Cu sample cell to consider about pressure dependence of heat capacity in Teflon sample cell. Using this type of sample cell, it can be measured free from subtracting such a pressure dependence of heat capacity. The dimensions of the cylinder were 8.8, 2.7 and 21mm in outer diameter, inner diameter and length, respectively. As a piston and piston backups, we used ZrO_2. The mixture of Fluorinert FC70:FC77=1:1 was used as a pressure transmitting media. It is estimated the pressures by the change of superconducting transition temperatures of Sn with the commercial SQUID magnetometer.

The total heat capacities are measured, which includes several parts of micro cell, pressure transmitting media and sample as a function of temperature below 4 K under the high pressure for single crystalline Ce_2RhIn_8. Ce_2RhIn_8 is well known Kondo material, which shows superconductivity

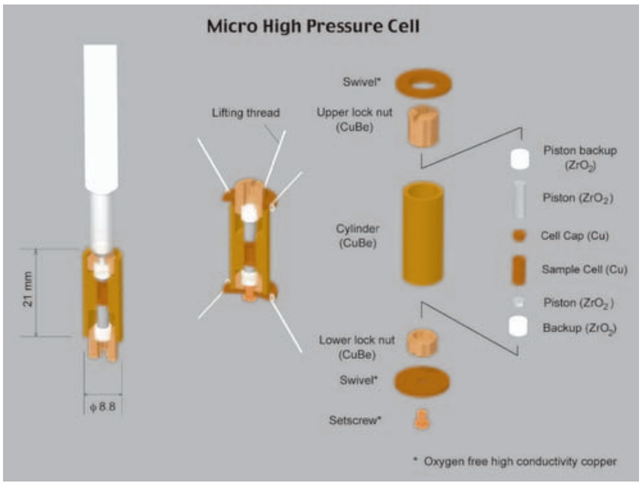

Fig. 1. Schematic drawing of new micro pressure cell

under high pressure. [2] The applied pressures are 0, 0.28, 0.43, and 0.57 GPa, respectively. In the case of Ce_2RhIn_8 measurements, the weight of sample is only about 40 mg. This value is less than 0.5% comparing to that of pressure cell. It is subtracted heat capacities of micro cell and pressure transmitting media from total heat capacity in order to obtain net heat capacities of sample under pressure. For this subtraction, we have already measured the heat capacities of pressure transmitting media under various pressures.

Figure 2 shows the specific heat of Ce_2RhIn_8 under pressures. It is clearly seen Néel temperature (T_N) of 2.8 K at ambient pressure. T_N decreases monotonically increasing pressure. Néel temperatures are estimated to be 2.5 K at 0.28 GPa, 2.2 K at 0.43 GPa, respectively. At 0.57 GPa, we can not observe any transition above 1.7 K. Magnetic contribution of specific heat around T_N is also decreases increasing pressure, which means the magnetic entropy decreases under high pressures. Estimated magnetic entropy are 1.7 J/K mol-Ce at 0 GPa, 1.3 J/K mol-Ce at 0.28 GPa and 1.2 J/K mol-Ce at 0.43 GPa, respectively.

We are now expanding these measurements to lower temperatures using ^{3}He cryostat and higher pressures to observe superconductivity of Ce_2RhIn_8.

References

[1] I. Umehara et al. to be published.
[2]M. Nicklas et al., Phys. Rev. B. **67** (2003) 020506.

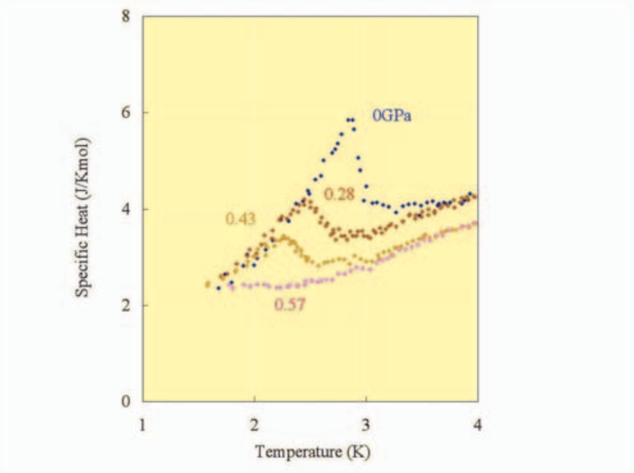

Fig. 2. The specific heat for Ce_2RhIn_8 as a function of temperature under the various pressures.

Authors
Izuru Umehara[a], Fumiaki Tomioka[a], Tetsuya Fujiwara, Masato Hedo, and Yoshiya Uwatoko
a*Dibision of Physics, Faculty of Engineering, Yokohama National University, Yokohama 240-8501*